

VolcashDB: Volcanic ash particle image and classification database

Damià Benet^{1,2}, Fidel Costa^{1,2,3}, Christina Widiwijayanti^{1,2}, John Pallister⁴, Gabriela Pedreros⁵, Patrick Allard³, Hanik Humaida⁶, Yosuke Aoki⁷

¹ Asian School of the Environment, Nanyang Technological University, Singapore

² EOS, Earth Observatory of Singapore, Nanyang Technological University, Singapore

³ Institut de Physique du Globe de Paris, Université Paris Cité, Paris, France

⁴ Volcano Disaster Assistance Program, U.S. Geological Survey, Vancouver, WA, United States

⁵ Observatorio Vulcanológico de los Andes del Sur, Servicio Nacional de Geología y Minería, Temuco, Chile

⁶ BPPTKG (Balai Penyelidikan dan Pengembangan Teknologi Kebencanaan Geologi), PVMBG, Geology Agency, Indonesia

⁷ Earthquake Research Institute, The University of Tokyo, Tokyo, Japan

This is a non-peer reviewed paper uploaded to EarthArXiv

We welcome your feedback!

damia001@e.ntu.edu.sg

Abstract

Volcanic ash provides unique pieces of information that can help understand the progress of volcanic activity at the early stages of unrest and possible transitions towards different eruptive styles. Ash contains different types of particles that are indicative of eruptive styles and magma ascent-related processes. However, classifying ash particles into its main components is not straightforward. Diagnostic observations vary depending on the magma composition and the style of eruption, which leads to ambiguities in assigning a given particle to a given class. Moreover, there is no standardized methodology for particle classification, and thus different observers may infer different interpretations. In order to help improving this situation, we created the web-based platform Volcanic ash DataBase (VolcashDB). The database contains > 6,300 multi-focused high-resolution images of ash particles as seen under the binocular microscope from a wide range of magma compositions and eruptive styles. We quantitatively extracted multiple features of shape, texture, and color in each particle image, and petrologically classified each particle into one of the four main categories: free crystal, altered material, lithic, and juvenile. VolcashDB is publicly available and enables users to browse, obtain visual summaries, and download the images with their corresponding labels, and thus could be used for comparative studies. The classified images could also be used to train Machine Learning models to automatically classify particles and minimize observer biases.

1.1 Introduction

With about 800 million people around the globe threatened by volcanic eruptions (Loughlin et al., 2015), volcanologists have tried for long to answer to basic questions of when, where, and how big the next eruption is going to be. The main approach to anticipating and tracking the evolution of eruptions has been the monitoring of geophysical signals (e.g., seismicity, ground deformations; Chouet, 2003; Dzurisin, 2006), as well as the composition and flux of gas emissions (e.g., Aiuppa, 2015). However, many volcanoes worldwide remain poorly monitored instrumentally, which hampers accurate interpretation of the processes occurring at depth and makes forecasting uncertain (Doyle et al., 2014; Newhall and Punongbayan, 1996).

An additional piece of information that can be used to address these challenges is studying the characteristics of emitted volcanic ash particles. The occurrence of ash emissions already implies ongoing eruptive activity but the latter can widely vary in origin and style over time, from minor discrete phreatic events, to larger phreatomagmatic outbursts, up to powerful magmatic eruptions (e.g., Gaunt et al., 2016; Gunawan et al., 2019). Transitions of eruptive sources and styles can happen in a temporal sequence during one single eruption at a given volcano (Bebbington and Jenkins, 2019). Because the characteristics of ash particles depend on both the nature of their rock source(s) and the mechanisms of fragmentation and ascent, ash monitoring can give clues to anticipate future changes in eruptive activity, even

before magma arrival at the surface (Benet et al., 2021; Suzuki et al., 2013). In particular, adequately identifying the occurrence of so-called juvenile magmatic particles in volcanic ash can provide crucial indication of fresh magma nearing, which bears important implications for hazard assessment and emergency planning during a volcanic crisis (Hincks et al., 2014).

The traditional approach to classify ash particles is through visual observations of their color, texture, and shapes under the binocular (Gaunt et al., 2016; Miwa et al., 2013; Pardo et al., 2014), and of particles' external surface and internal microstructures in the scanning electron microscope (SEM; D'Oriano et al., 2014; Pardo et al., 2020). These observations are sometimes complemented by further chemical analyses with electron microprobe, mass spectrometry, or spectroscopic analysis (Rowe et al., 2008). However, classifying ash particles into their different components (e.g., juvenile or lithic) is not always straightforward. A given component can include ash particles that widely range in shapes and colors, and the classification criteria are often valid on a case-by-case sample basis. Moreover, there is no standardized set of observations to discriminate between particle types, making classification subject to various interpretations depending on the observers. This can lead to inconclusive evidence for discrimination (e.g., Mt. Tongariro, 2012; Pardo et al., 2014), and/or contradicting classification of particles by different observers, which has had critical implications for hazard assessment (e.g., Soufrière de Guadeloupe, 1975–1977, Feuillard et al., 1983).

To begin to address this problem we created a Volcanic ash DataBase (VolcashDB). This is a web-based platform aimed at hosting a curated dataset of particle images and extracted features from a range of eruptive styles that have already been classified. Such dataset could be used for comparative studies between eruptions. It could also serve as a basis for automatic, objective classification of ash particles by applying machine learning, as has been done in several fields (He et al., 2015), as well as in geological sciences for sand particles (Li and Iskander, 2022), mineral grains (Latif et al., 2022, Maitre et al., 2019), and even for classification of shapes of volcanic ash (Shoji et al., 2018).

1.2 Data acquisition, labeling of particles, and errors

To obtain the images and characteristics of ash particles that constitute VolcashDB we used the following steps: i) sample preparation, ii) particles image acquisition and processing, iii) feature extraction, iv) classification by the petrologist, and v) data archiving (Figure 1).

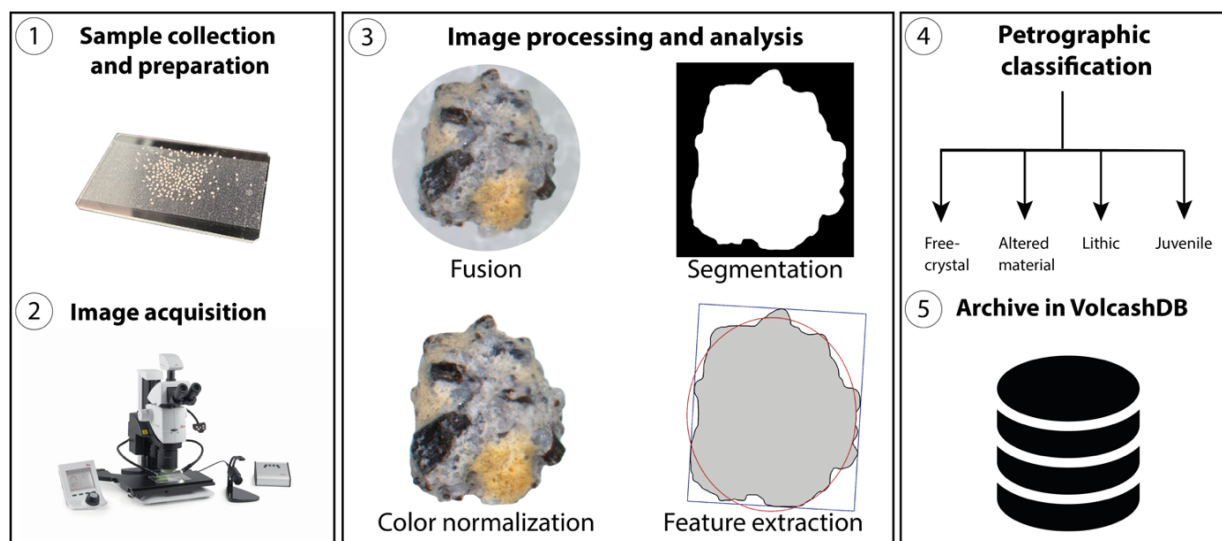


Figure 1: Methodology used to obtain the images and extract the particle's features that make the contents of VolcashDB. (1) ash particles are spread on a glass slide, (2) a scan of each slide with many images of individual particles is obtained using a binocular scanning stage (3) the scans are processed by image fusion, segmentation and color normalization, and analyzed by extracting 33 features related to the shape, texture and color. (4) each particle's image is classified by the petrologist, and (5) the particle's image, its main characteristics, and its classification are stored in the database which are shared in a public web-based platform.

1.2.1 Laboratory procedures and image acquisition

The samples were cleaned ultrasonically in cycles of 15 seconds to avoid glass shard damage, dried overnight at 60 °C, and sieved using four meshes of pore-size $\phi 0$, $\phi 1$, $\phi 2$ and $\phi 3$. We prepared multiple glass slides for a given sample, each consisting of 100 to 300 individual particles, from the coarser available grainsize fraction (mostly $\phi 0$ – $\phi 1$). Particles were deposited on top of a transparent, 3M 9415PC Removable Repositionable Tape that was glued on a glass slide of standard dimensions (75 mm by 25 mm). To improve the separation of individual particles on the slide, we used a mesh of a finer pore size than the particle's size of interest. We also manually separated any touching particles with a needle.

The glass slide was then positioned on top of an opaque, white plate, and automatically scanned using a binocular microscope and stage system by Leica

(LMT260 XY Scanning Stage) equipped with the Leica LAS X imaging software available at Nanyang Technological University (NTU), Singapore. We used a Leica AX carrier to obtain 25 aligned scans at different focal depths to visualize the morphology of the particles top-to-bottom. The imaging software conditions to scan the ϕ_0 - ϕ_1 , ϕ_1 - ϕ_2 and ϕ_2 - ϕ_3 fractions were at 5x, 6x and 8x magnifications, exposure values of 95, 105 and 120, without gain. This procedure is relatively fast, with acquisition times between 25 to 45 minutes for each glass slide, although the high-resolution scans (typically around 25,000 x 35,000 pixels) and associated temporary files can be up to 140 GB per slide. The scanned glass slides were then stored for reproducibility purposes. We also observed one slide per sample using a JEOL JSM-7600F Scanning Electron Microscope (SEM at NTU) to aid particle identification (see section 1.2.6 for more detail). Operating conditions for the SEM analysis were at low vacuum (50 MPa), 15 kV of accelerating voltage, 8 nA of probe current, at a working distance of 20 mm. We used a pixel resolution of 1024 x 2048, obtaining about 5×10^6 pixels per particle of the exported images, and dwell time of 60 s.

1.2.2 Image processing

We processed the scans of the images in three steps: image fusion, image segmentation, and color normalization (Figure 1). With this procedure, we obtained multi-focused, segmented, and normalized particle images which are the main type of images in VolcashDB, abbreviated as MSNI. The steps were automated with a

Python program that was run using the Gekko cluster at the Nanyang Technological University (NTU) High Performance Computing Center.

Image fusion consists of combining focused regions from multiple images of the same 3D object into one 2D array to obtain a multi-focused image. We fused the scans using the open-source model SESF-Fuse of Ma et al. (2021) which uses Deep Learning (DL) and has been pretrained using tens of thousands of images. The training set consists of pairs of images that either have blurry foreground and focused background, or vice versa. The model is trained to produce a fully focused image (Ma et al., 2021) and is freely downloadable in GitHub (<https://github.com/Keep-Passion/SESF-Fuse>). To decrease the run time, we split each scan into ten smaller arrays and ran them separately, obtaining an overall run time per scan of <3 hours with ~90% of the images fused.

The multi-focused scans were then segmented using the open-source, DL model named U²-NET by Qin et al. (2020). This model is grounded on about 20,000 images of single or multiple objects which are positioned in front of a background with variable textures and colors, and it automatically produces a binary mask where background pixels take a value of zero while the object of interest gets a value of one. To run U²-NET on our dataset, we split the multi-focused scans (10–40 kilopixels square) into smaller arrays (e.g., 5,000 × 1,000 pixels), obtaining run times between 5–7 days with ~80% of the particles properly segmented. Upon completion of this

process, we obtained multi-focused images of individual particles with resolutions of $\sim 2.5 \times 10^6$ pixels per particle image (pxls/p) and $\sim 1.9 \times 10^6$ pxls/p for the grain-size fractions ϕ_0 – ϕ_1 and ϕ_1 – ϕ_2 . As we discuss later in section 1.2.8 about uncertainties, the segmentation algorithm by Qin et al. (2020) may not capture microscale irregularities (e.g., $<10 \mu\text{m}$ vesicles) of the particle outline at the image resolution we used, which may affect the values of the extracted shape features.

1.2.3 Color normalization

Variations in the background brightness can be measured by pixel intensity and is subject to changes in experimental conditions, such as scan magnification and environmental light. We used the same white opaque plate as a background to obtain all the images, and as calibration to normalize the particle images. We rescaled all image pixels to a background of pixel intensity of 200 (the pixel scale color varies from 0 to 255) to accommodate pixel values that are brighter than the background (e.g., crystal reflections). After this step, we obtained about 6,300 multi-focused, segmented and normalized images. About 6% of images that contained artefacts and were manually discarded.

1.2.4 Quantitative feature extraction from the images

We extracted 33 key features from every ash particle image which are related to shape, texture, and color. As described below in more detail, we measured shape features that are common in previous studies of volcanic ash (Cioni et al., 2014; Dellino and La

Volpe, 1996; Leibbrandt and Le Pennec, 2015; Liu et al., 2015). An extensive compilation of the shape parameters and how their calculation depends on the authors' methods can be found in Dürig et al. (2018). For textural analysis, we measured the Grey Level Co-occurrence Matrices (GLCMs) as proposed by Haralick et al. (1973), which computes the degree of similarity and/or dissimilarity of the grayscale pixel distribution. We analyzed the color distribution by computing the histograms of various channels, and retrieved their descriptive statistics, including the mean, standard deviation, and mode. These steps of feature extraction were automated with a Python program that uses various functions from the open-source package Scikit-image. This program was run on the Gekko cluster of the High-Performance Computing Center at NTU.

Shape features

To compute shape features it is necessary to first measure some basic morphological properties (Figure 2, Table 1). We retrieved the particle outline from the binary segmented image (Figure 1) and with Scikit-image's function `regionprops` we measured the following series of parameters: the particle area and perimeter, the area and perimeter of the hull (the minimum area that bounds the particle outline), the width and height of the bounding rectangle, the Feret maximum diameter which is the maximum distance between two parallel lines tangential to the particle outline, and the major ellipse axis (E_{maj}) which is the longest perpendicular axis of the enclosing ellipse (Dürig et al., 2018). These morphological properties were then used

to calculate the following shape features (Table 2): solidity, convexity, elongation and roundness (Liu et al., 2015), circularity (named *circ_dellino*), rectangularity and compactness (Dellino and La Volpe, 1996), circularity (named *circ_cioni*; Cioni et al., 2014), and aspect ratio (Leibrandt and Le Pennec, 2015).

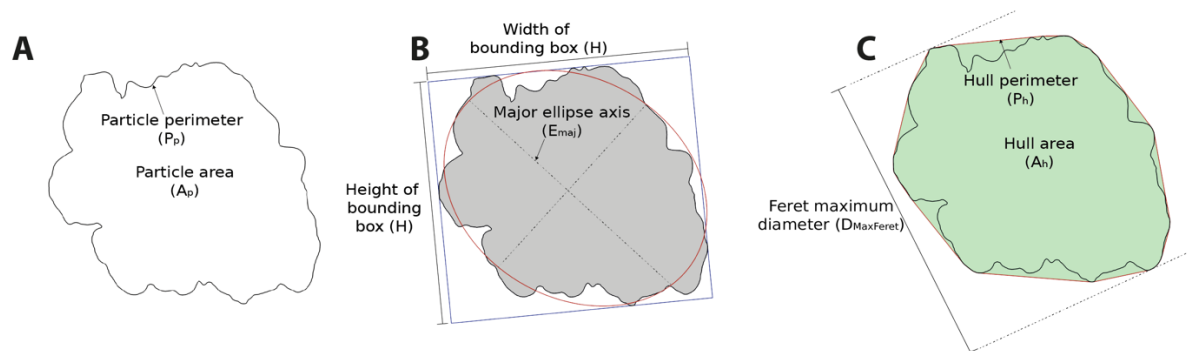


Figure 2: Illustration of the measured particle properties to extract shape features listed in Table 2. We use the binary mask obtained after segmentation (see in Figure 1), to retrieve the outline of the particle. The outline is inputted to Scikit-image's function *regionprops* to measure (A) the particle area and parimeter, (B) the bounding box and major ellipse axis, and (C) the Feret maximum diameter and the hull.

Table 1: List of abbreviations of the measured properties used in the equations for feature extraction (Table 3.2).

Symbol	Definition	Reference
Shape		
A_p	particle area	1
P_p	particle perimeter	1
A_h	hull area	1
P_h	hull perimeter	1
W	width of bounding rectangle	1
H	height of bounding rectangle	1
$D_{MaxFeret}$	Feret maximum diameter the maximum distance between two parallel lines tangential to the particle outline	1
E_{maj}	major ellipse axis	1
Texture		
$levels$	pixel intensities from the ROI used for GLCM calculation	2
i, j	i is the origin pixel, whereas j is the target pixel	2
$P_d^\theta(i, j)$	It is the $(i, j)^{th}$ entry in the GLCM (see ‘Texture features’ in this section for its definition and Figure 3.3 for an example), and represents the probability of pixel pairs at a given distance (d) and angle (θ)	2
μ_i	GLCM mean	2
σ_i^2	Variance	2
Color		
N	Total number of pixels	–
x_i	Pixel value	–
\bar{x}	Mean of pixel values	–

¹ Dürig et al., 2018 and references therein.

² Hall-Beyer, 2017.

Table 2: Extracted features and equations to calculate them.

Feature	Equation	Reference
Convexity	P_h/P_p	Liu et al., 2015
Rectangularity	$\frac{P_p}{2H+2W}$	Dellino and La Volpe, 1996
Elongation	$\frac{D_{MaxFeret}^2}{E_{maj}}$	Liu et al., 2015
Roundness	$\frac{4A_p}{\pi D_{MaxFeret}^2}$	Liu et al., 2015
Circ_dellino	$\frac{P_p}{2\sqrt{\pi A_p}}$	Dellino and La Volpe, 1996
Circ_cioni	$\frac{4\pi A_p}{P_p^2}$	Cioni et al., 2014
Solidity	$\frac{A_p}{2H + 2W}$	Liu et al., 2015
Aspect_Rat	W/H	Leibrandt and Le Pennec, 2015
Compactness	$\frac{A_p}{HW}$	Dellino and La Volpe, 1996
Contrast	$\sum_{i,j=0}^{levels-1} P_d^\theta (i-j)^2$	Hall-Beyer, 2017
Dissimilarity	$\sum_{i,j=0}^{levels-1} P_d^\theta i-j $	Hall-Beyer, 2017
Homogeneity	$\sum_{i,j=0}^{levels-1} \frac{P_d^\theta(i,j)}{1+(i-j)^2}$	Hall-Beyer, 2017
ASM	$\sum_{i,j=0}^{levels-1} P_d^\theta(i,j)^2$	Hall-Beyer, 2017
Energy	\sqrt{ASM}	Hall-Beyer, 2017
Correlation	$\sum_{i,j=0}^{levels-1} P_d^\theta \left[\frac{(i-\mu_i)(j-\mu_j)}{\sqrt{(\sigma_i^2)(\sigma_j^2)}} \right]$	Hall-Beyer, 2017
Channel ¹ mean	$\frac{1}{N} \sum_{i=1}^n x_i$	Maitre et al., 2019
Channel standard dev	$\sqrt{\frac{1}{N-1} \sum_{i=1}^N (x_i - \bar{x})^2}$	Maitre et al., 2019

Channel mode	Computationally found as the most common value in the array by Scipy's <i>stats.mode</i> function	e.g., Mehbodniya et al., 2022
--------------	---	-------------------------------

Texture features

We used Gray Level Cooccurrence Matrix (GLCM; Haralick et al., 1973) to extract features related to texture (Table 1 and Table 2). The images were transformed from RGB to grayscale (one single channel with pixel values ranging from 0 to 255) and rescaled to a maximum pixel value of 15 to make the computations faster. The images were then cropped into several regions of interest (ROI), radially distributed from the particle center, with sizes between 100–300 squared pixels and without the inclusion of background (Figure 3). For each ROI, we computed the GLCM. Each element in the GLCM is defined by the frequency at which the value of a “starting” pixel repeats respect the value of a “target” pixel. The spatial relation between the two pixels is defined by an angle (θ) and distance (d ; see a simplified example in Figure 3; Singh et al., 2017). To obtain the GLCM, the frequency is calculated by every possible pair of pixel values. We used several angles at steps of 11.25° and up to six different distances, obtaining a maximum of 90 GLCMs per ROI. For every individual GLCM, we calculated the contrast, dissimilarity, homogeneity, Angular Second Moment (ASM), energy and correlation proposed by Haralick et al. (1973), using Scikit-image's functions *graycoprops* and *graycomatrix* (see Hall-Beyer, 2017 for a comprehensive tutorial). We averaged across GLCMs and ROIs to obtain one final value of the textural

features per image. Textural features computed from GLCM have been previously used for mineral classification of rock thin sections (Pereira Borges and Aguiar, 2019).

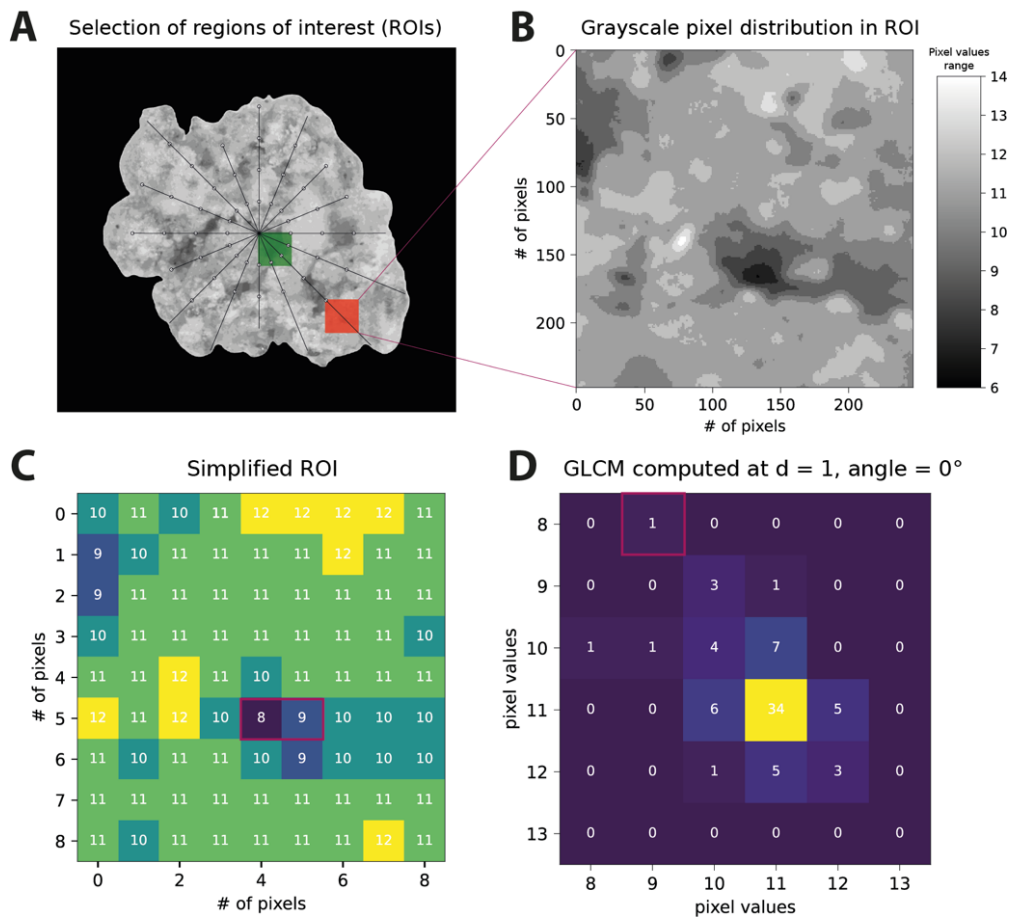


Figure 3: Calculation of the Gray Level Co-occurrence Matrix (GLCM) in four steps. (A) Starting from the particle center (green square), an array of Regions of Interest (ROIs) is defined concentrically and within the particle outline. (B) Each ROI is rescaled to pixel values between 0 and 16 to improve the computational efficiency. This specific ROI has a range of pixel values from 6–14. (C) Simplified image of that shown in (B) expressed as a matrix, with a green map for contrast, where each pixel contains its own value in the center. (D) Calculation of the GLCM based on the pixel distribution of (C) at a distance (d) equal to 1, and angle equal to 0° . To calculate the

number of pairs between 8 and 9, i.e., the element (8,9) in the GLCM outlined in red in (D), the algorithm checks whether a 9 is found right next ($d=1$) to an 8 at 0° (i.e., at the right-hand side). As there is only one occurrence (C; red rectangle), the element (8,9) of the GLCM takes a value of 1. Following the same process, the algorithm finds 34 occurrences (squared in yellow in diagram D) of 11 being on the right side of 11 in (C). This process is performed for every possible pixel combination at various depths and angles, obtaining an array of GLCMs, from which texture features listed in Table 2 were calculated.

Color features

For each image we extracted color features from two color spaces (Figure 4): (1) Red, Green and Blue (RGB), and (2) Hue, Saturation, and Value (HSV). The RGB space is based on the red, green, and blue additive primaries, and it is commonly used for images captured with a camera, where pixels range from 0 to 255 (Ibraheem et al., 2012). The HSV space was inspired by how the human eye perceives the color, i.e., separating color information from intensity. Hue refers to the chromaticity, i.e., the color information, the saturation relative to the color purity and intensity, whereas the value describes the brightness, which is perceived to the human eye as luminance (Ibraheem et al., 2012; Sural et al., 2002). We used as many bins as pixel values to convert the two-dimensional channels to histograms (i.e., 256, except for the hue, which has a range from 0 to 179). Then, we computed the mean, mode, and standard

deviation of the histograms as color features, as has been previously done for recognition of mineral grains (Table 1 and Table 2; Maitre et al., 2019).

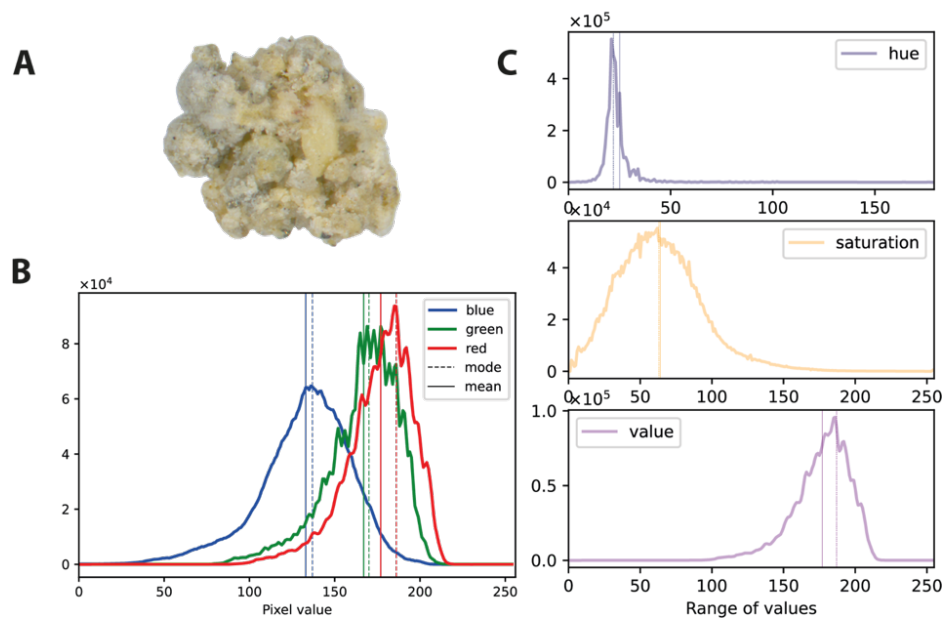


Figure 4: Figure 4. Since a colored image (A) is made of three two-dimensional arrays (the Red-Green-Blue channels), histograms (B) can be obtained by flattening each array into a one-dimensional vector. Additionally, we transformed the RGB image into the Hue-Saturation-Value (HSV) space and obtained in the same way the associated histograms (C). The extracted color features consist of the mean, mode and standard deviation of the six RGB and HSV channels, following the equations in Table 2.

1.2.5 Main observed characteristics of the particle images

When observing the particle images under the binocular and SEM, we paid special attention to several particle characteristics (Table 3). These include color, luster, shape,

and texture, and have been used in the literature as classification indicators as explained in more detail in paragraphs below.

Table 3: List of observations, attributes, and in brackets and lower-case, the abbreviations used for labelling each particle image (see Table 3.5).

	Binocular				SEM-EDS				
Color	Transparent (tr)	Black (bl)	Yellowish	White	Pitting	Absent	Low	Medium	High
Luster	Glossy	Vitreous	Metallic	Dull	Glass greyscale	Homogeneous Heterogeneous			
Alteration¹	Absent (n)	Low (l)	Medium (m)	High (h)	Glass composition	Homogeneous Heterogeneous			
Shape	Blocky (b)	Fluidal (f)	Spongy (s)	Others ²	Iron oxides lineation	Yes	No		
Surface	Smooth	Rough							
Edges	Angular	Subangular	Subrounded	Rounded					
Crystallinity	Low (lc)	Medium (mc)	High (hc)						
Vesicularity	Absent	Low	Medium	High					

¹Alteration refers specifically to the degree of hydrothermal alteration

²Others include highly-vesicular (hv), microtubular (mt) and pumice-like (p) shapes.

We identified a variety of particle colors qualitatively, and some of the most common include “transparent” (Figure 5A), black or dark grey (Figure 5I–J), white (Figure 5H), and reddish (Figure 5E) to yellowish (Figure 5F); the latter two are typical of hydrothermally altered material (e.g., Minami et al., 2016). The reported colors may vary with the eyesight of the observer, which in this case he (D. Benet) was found not to be color-blind according to a web-based test (<https://eu.enchroma.com/pages/colour-blind-test>). The luster has been shown to be

critical for recognizing juvenile particles (D’Oriano et al., 2014; Gaunt et al., 2016; Miwa et al., 2013), as such particles are typically glossy (Figure 5M–P). In addition, we also identified particles with dull (Figure 5I–J), vitreous (Figure 5A), and waxy (Figure 5G) lusters.

We qualitatively categorized the particles edge angularity into: (i) angular (Figure 5N), (ii) subangular or subrounded (Figure 5M), and (iii) rounded or well rounded (Figure 5H), following the visual comparison chart of Russell, Taylor and Pettijohn (Müller, 1967; see Figure S3.1 in the supplementary materials). These categories are important for particle classification, as those with rounded edges could have been weathered, whereas those with angular, sharp edges might be fresh. Various terms have been proposed to describe the particle shapes depending on the author (e.g., Heiken and Wohletz, 1985). Here, we used blocky (Figure 5M) for relatively equant particles with perpendicular to sub-perpendicular edges, fluidal if smooth-surfaced with rounded walls (Figure 5P), spongy for particles that contain abundant and relatively small vesicles, highly-vesicular (Figure 5N) where vesicles are less abundant but larger in size, microtubular, where particles contain elongated hollows, and pumice-like (Figure 5O) where the groundmass contains ubiquitous < 10 µm-sized vesicles. We also recorded the relative abundance of glass and crystals in the groundmass and classified it as: low crystallinity for 0–20% (Figure 5O), mid for 20–40% (Figure 5M), and high for crystallinities above >40% (Figure 5J). We note that here we refer only to groundmass microcrystallinity, i.e., excluding phenocrysts.

Main types	Image and label	Characteristics	Image and label	Characteristics	Image and label	Characteristics	Image and label	Characteristics	
Free-crystal	 A PG	<ul style="list-style-type: none"> •Transparent •Vitreous •Well-faceted •Planar structures 	 B PX	<ul style="list-style-type: none"> •Black •Well-faceted •Planar structures 	 C PX	<ul style="list-style-type: none"> •Green bottle •Vitreous •Well-faceted •Planar structures 	 D AMF	<ul style="list-style-type: none"> •Black •Well-faceted •Planar structures 	
	Altered material	 E AHh	<ul style="list-style-type: none"> •Red •Rounded •Granular •High hydrothermal alteration 	 F AHh	<ul style="list-style-type: none"> •Yellowish •Angular •High hydrothermal alteration •Aggregate 	 G AW	<ul style="list-style-type: none"> •Light gray •Waxy •Subrounded •Rough (dissolution?) surface 	 H AW	<ul style="list-style-type: none"> •White •Dull •Rough surface •Well rounded •Secondary minerals
		Lithic	 I LLblhcl	<ul style="list-style-type: none"> •Black •Dull •Subrounded •High crystallinity •Low hydrothermal alteration 	 J LLblhcn	<ul style="list-style-type: none"> •Black •Dull •Subrounded •High crystallinity •Unaltered 	 K LLtrlcn	<ul style="list-style-type: none"> •Transparent •Less shine than glossy •Subangular •Low crystallinity •Unaltered 	 L Lblhchvm
	Juvenile		 M JJtrmb	<ul style="list-style-type: none"> •Transparent •Glossy •Smooth •Subangular •Mid crystallinity •Blocky 	 N JJblhcv	<ul style="list-style-type: none"> •Black •Glossy •Smooth •Angular •Low crystallinity •Highly-vesicular 	 O JJtrlcp	<ul style="list-style-type: none"> •Transparent •Glossy •Smooth •Bubble wall •Low crystallinity •Pumice-like shape 	 P JHtrlcf

Figure 5: Examples of particle images with their main characteristics, their individual label (see Table 3 Table 4 for the meaning of labels), and the type they belong. Note that only some of the characteristics have been used as particle labels (*in italics*).

We categorized the amount of yellowish, reddish and white material adhered to the surface, typical of hydrothermal origin (e.g., Minami et al., 2016) as: absent, if free of hydrothermal coatings (Figure 5M–O); low, if the amount is very small (e.g., dust; Figure 5I); medium, when the coatings are abundant and may form encrustations (Figure 5L); and high, when the grain surface is entirely or almost entirely covered (Figure 5E). We paid attention to features indicative of weathering, including coatings

of white minerals (clays; Figure 5H), dissolution textures (Figure 5G), and evidence of recrystallization/devitrification. Moreover, for the particles observed under the SEM we also recorded the presence of pitting, a form of chemical alteration that generates micro-porosity, and also evidence of recrystallization, such as iron oxides lineations (D’Oriano et al., 2014).

1.2.6 Labeling of the particles by petrologist

Using the observational features noted above –not to confuse with the 33 extracted features–, each particle was classified into the four main types that are typically used in the literature (e.g., Gaunt et al., 2016; Suzuki et al., 2013; Ross et al. 2022): free crystals, altered material, lithic, and juvenile; we also classified the particles into a few sub-types (Table 4).

Table 4: List of main particle types and sub-types we have used in the database.

Main types	Sub-type
Free-crystal (F ¹)	Plagioclase (PL) Pyroxene (PX) Amphibole (AMF)
Altered material (A)	Weathered material (AW) Hydrothermally altered material (AH)
Lithic (L)	Standard lithic (LL) Recycled juvenile particles (LJ)
Juvenile (J)	

Standard juvenile
(JJ)
Syn-eruptively
hydrothermally
altered (JH)

¹In brackets and upper-case, the abbreviations used for image labelling (Table 5).

In addition, for each particle we noted special characteristics such as crystallinity degree, degrees of hydrothermal material, and shapes. We used a simplified four-step process to classify the particles into the main types and to provide a label with the appropriate abbreviation (Figure 5):

- (1) Identification of features that are characteristic of free crystals (*F*; Figure 5A–D).

These include planar structures (e.g., twinning) and well-faceted crystal habit. The free crystals in the database are mainly plagioclase and pyroxene, minor amphibole, and rarely native sulfur and olivine.

- (2) Altered material (*A*) includes both hydrothermally altered as well as weathered particles. We looked for and noted evidence of major hydrothermal alteration.

Particles that were partially or entirely covered by hydrothermal encrustations (medium or high degrees of hydrothermal alteration) were classified as hydrothermally altered (*AH*; Figure 5E–F). When visible, we also noted their crystallinity. These hydrothermally altered particles typically have granular texture or form aggregates that are white, or yellowish to reddish. After discarding free crystals and hydrothermally altered particles, most of the particles that are left are generally glassy and variably altered. At this point, we identified

features that are characteristic of weathered particles (*AW*; Figure 5G–H). Under the binocular, these include a loss in shine (dull luster), round edges, and modifications of the original groundmass, such as recrystallization into secondary minerals (typically whitish clays) and dissolution textures. Weathered particles are typically white, dull to waxy, and have rough surfaces. Particles containing weathering features at an early stage of development can be difficult to identify under the binocular microscope, and we recommend the observation of incipient palagonization, recrystallisation, and presence of secondary minerals by SEM.

- (3) Most lithic particles (*L*) are typically dull, dark, with sub-angular to rounded edges, and contain limited signs of weathering or hydrothermal alteration (absent to low degrees). We further noted their crystallinity, and whether they are transparent or black. Recycled juvenile (*LJ*), when observed under the binocular, often show a duller or metallic luster, sometimes with disseminated red patches (Figure 5L), but the SEM is necessary to observe conclusive features such as recrystallization and the presence of iron oxides aligned around microphenocrysts—features attributed by D’Oriano et al. (2014) to particles that fall back into the crater and are thermally altered in oxidizing conditions. Because we don’t know the time span between the LJ fall and their ejection, we classified them as lithic component to prevent overestimating the juvenile component.
- (4) Finally, we paid special attention to features that are characteristic of fresh, juvenile particles (*J*; Figure 5M–P). We mainly recorded five features, here referred as “fresh-like”. These are based on a review of 35 articles from the literature

(Figure 6) and include: shiny gloss, sharp edges, smooth-skinned surface, and lack of weathering and alteration features (Figure 5M–O). We avoided using specific names such as sideromelane and tachylite because these may have connotations related to the chemical composition (e.g., Taddeucci et al., 2004). We also noted the particles' shape to detect temporal changes and the appearance of new shape types, such as the occurrence of vesicular particles. The presence of juvenile particles in volcanic ash is typically interpreted as evidence for shallowly emplaced magma, which has critical implications for hazards assessment. We thus also observed these particles using the SEM. We looked for homogeneous grayscale, smooth surface, sharp or stepped edges (Pardo et al., 2020; Ross et al., 2022), and the lack of signs of weathering (e.g., etch pitting). Juvenile particles were further classified based on crystallinity and color, and based on the shape and presence of hydrothermal material on surfaces. Hydrothermally altered juvenile particles (JH) are classified as a subgroup, and are characterized by incipient and limited amount of hydrothermal coatings together with characteristics that strongly point towards a juvenile origin (e.g., the appearance of vesicular shapes). These are interpreted to form by syn-eruptive alteration of juvenile material by hot hydrothermal fluids with juvenile material (Alvarado et al., 2016) or by interaction with plume gases (Spadaro et al., 2002).

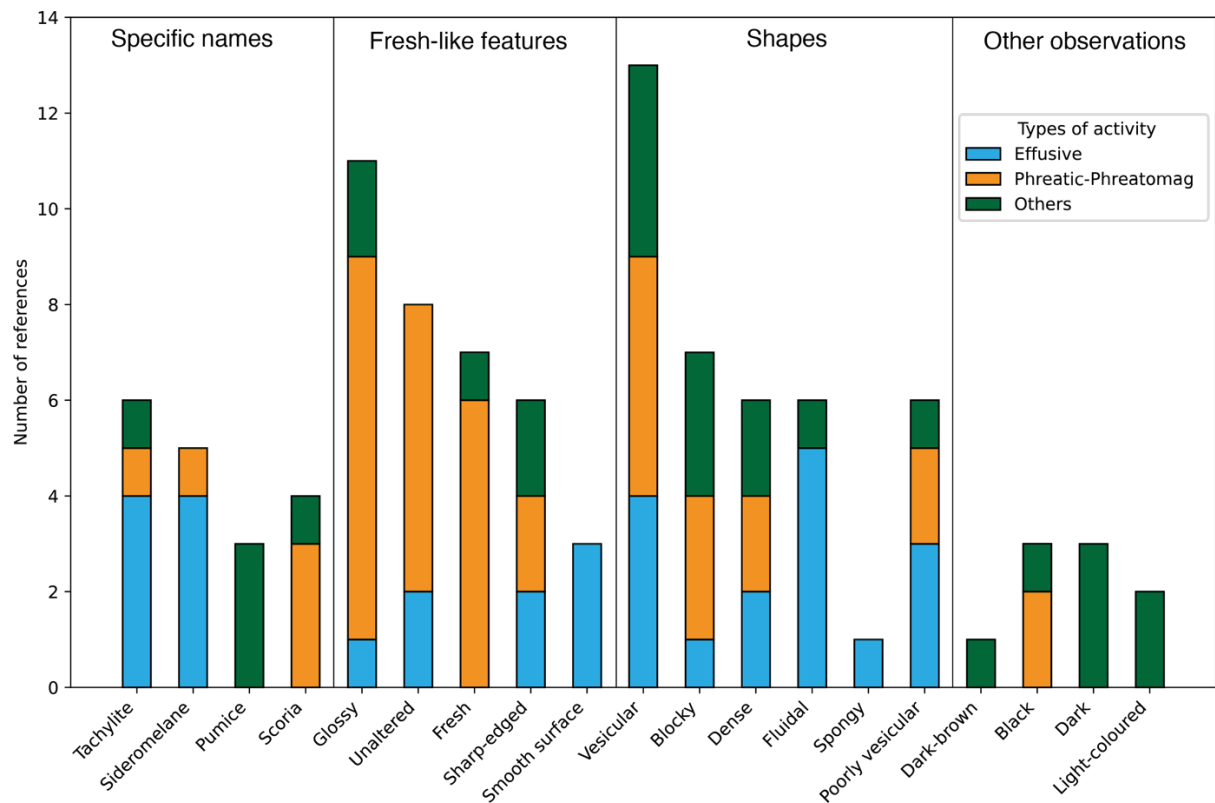


Figure 6: Main characteristics of juvenile particles observed under the binocular microscope according to the previous publications on a range of volcanic eruptions. Most observations are from effusive from basaltic compositions, phreatic and phreatomagmatic explosions of intermediate to acid compositions, and into the category 'Others', which includes subplinian, plinian and submarine eruptions. Data sources: Andronico et al., 2014, 2013; Angkasa et al., 2019; Battaglia et al., 2019; Benet et al., 2021; Cioni et al., 1992; D'Oriano et al., 2022, 2014, 2011, 2005; Ersoy, 2010; Ersoy et al., 2006; Eychenne et al., 2015; Gaunt et al., 2016; Geshi et al., 2016; Gómez-Arango et al., 2018; Gorbach et al., 2018; Houghton and Smith, 1993; Kurniawan et al., 2017; Lücke and Calderón, 2016; Matsumoto and Geshi, 2021; Minami et al., 2022; Miwa et al., 2021, 2013; Miyabuchi et al., 2018; Miyagi et al., 2020; Pistolesi et al., 2021; Romero

et al., 2020; Savov et al., 2008; Scasso and Carey, 2005; Suzuki et al., 2013; Taddeucci et al., 2002; Thivet, 2020; Troncoso et al., 2017; White and Houghton, 2006

The particles are labelled with a sequence of letters (Table 3) that reflect the types and sub-types (Table 4), and are occasionally followed by lower case letter(s) that are the abbreviation(s) of some of the special characteristics that we have decided to record (Table 5).

Table 5: Examples of individual particle labels made of a sequence of letters that represent the abbreviations of the main particle type (Table 4) and some of their characteristics (Table 3). Note that the abbreviations are separated by a dash to improve the readability, but these are not present in the labels of the database.

Particle label	Meaning
PG, PX, AMF	Plagioclase, pyroxene, amphibole
AW	Weathered material
AH-h	Hydrothermally altered material-high degree of hydrothermal alteration
AH-bl-hc-m	Hydrothermally altered material-black-high crystallinity-medium degree of hydrothermal alteration
JJ-bl-hc-b	Juvenile-black-high crystallinity-blocky
JH-tr-lc-l-s	Hydrothermally altered juvenile-transparent-low crystallinity -low degree of hydrothermal alteration-spongy
LL-tr-mc-n	Lithic-transparent-medium crystallinity-absent hydrothermal alteration
LJ-bl-lc-f-m	Recycled juvenile-black-low crystallinity-fluidal-medium degree of hydrothermal alteration

1.2.7 Uncertainties and errors in particle proportions and classification

Several types of uncertainties and errors play a role on the precision and accuracy of our measurements and particle classification. Precision describes the variability and spread of the experimental data, and it can be quantified with the standard deviation, whereas the accuracy relates to the difference between the experimental values and the true value (which is often unknown). We assume that errors that influence the precision are random, whereas those influencing the accuracy are systematic (e.g., Hughes et al., 2010).

Uncertainties in ash componentry

Ash componentry studies report the proportions of the different particle from the analysis of a given number of particles from an assumed homogeneous subsample or aliquot. The reported proportion of particles have errors that depend on: (1) the number of particles that are counted and corresponds to the precision of the measurements, and (2) on the misclassification of particles, which corresponds to the accuracy of the measurements.

The error related to the precision can be assumed to be random and varies according to the number and proportion of the particle types that are observed. The proportion (p) is the ratio between the number of a particle type and the total number of particles, and it can be reported in percentage or in decimal form. This error can be expressed as the margin of error (ME ; e.g., Tanur, 2011), where it is assumed that the particles of

a sample are selected randomly, and that the proportion in the sample is normally distributed. The *ME* is quantified with a confidence level that is associated with a *z*-score (z_i , which is obtained from the area under the gaussian curve, e.g., Mendenhall et al., 2012), a standard deviation (σ), and population size (n ; the total number of particles measured for a given sample):

$$ME = z_i \sqrt{\frac{\sigma^2}{n}} \quad (1)$$

where we calculate the standard deviation as: $\sigma = \sqrt{p(1-p)}$ (Mendenhall et al., 2012). For example, for a 95% confidence level (i.e., $z_i=1.96$) and a measured proportion of 10% ($p=0.1$) in a total of 400 particles, we obtain that $\sigma = 0.3$, hence, $ME = 1.96\sqrt{0.3^2/400} = 0.03$, which corresponds to 3%. This means that obtained proportion will be within the interval $10\pm 3\%$, from which we can calculate the relative error to be $3/10$, or 33%. There is a trade-off between the number of particles that we count and the precision that we need to make useful characterization of the sample componentry (Liu et al., 2017; Ross et al., 2022). Thus, we made some model calculations of the relationship between the number of particles, their proportions and the precisions that we would obtain for a 95 % confidence level (Figure S3.2). For example, if we wish a relative error $< 30\%$, for a particle type with a proportion larger than 20%, we need to measure at least 200 particles (Figure S3.2). However, if we are dealing with a particle type that occurs in a low proportion such as about 1%, and we wish a relative error $< 100\%$ we need to measure at least 400 particles (Figure S3.2).

Particle classification errors and accuracy

The errors related to the accuracy are much more difficult to quantify because we do not know a priori the true particle types. These can be random, as when the observer misclassifies a particle because the image is partly blurry or because of ambiguity of observations, or they can be systematic, when the observer systematically misclassifies particles from a given type into another. We have tried to quantify the random but non-systematic errors by classifying the particles from two aliquots of the same sample, which could in principle reflect the incorrect classification by the observer due to random errors. The expectation is that, if the misclassification errors are small, the difference in the particle proportions between the two aliquots should be within the precision of the measurements as explained above. We did such exercise for ash samples of Kelud (2014) and Soufrière de Guadeloupe (1976; Figure 7); we found that the particles proportions from the two aliquots are within the margin error, which suggests that the effect of random errors in particle misclassification is small and thus not significant.

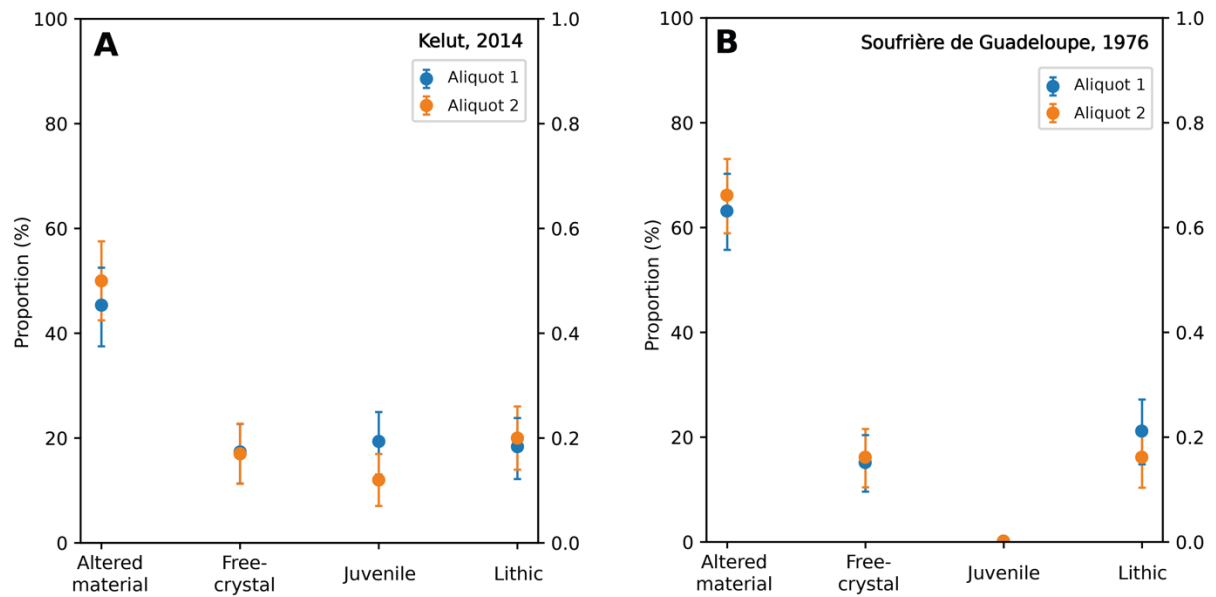


Figure 7: Particles' proportions of two aliquots (in blue and orange) from two ash samples to test the effect of random errors from misclassification of particles. A total of 170 particles were measured for each aliquot. (A) Kelud, 2014 and (B) Soufrière de Guadeloupe, 1976. The relative error (ME) of the proportions for each particle type overlaps, from which we infer that the random error in particle misclassification is not very significant, and smaller than the ME.

Quantifying the accuracy for systematic errors of particle misclassification is difficult, as we don't know the true particle types, and although some particles have unequivocal traits for classification, others show inconclusive features. For example, classifying particles such as crystals, can be done with clear diagnostic observations such as cleavage, but classifying particles with limited signs of weathering as lithic or weathered material is not obvious, and will likely vary with the observer. We strived to limit the problems of misclassification by adopting the same observational characteristics of particles reported in the literature, especially for juvenile particles

(Figure 6). Proper quantification of the accuracy or misclassification could be done by expert elicitation procedures (e.g., Aspinall and Cooke, 1998; Marzocchi and Bebbington, 2012), where several experts classify the particles from the same sample, but this is currently beyond the scope of this contribution.

1.2.8 Uncertainties and errors in feature extraction

Our binocular images of individual particles are high-resolution (between 10^6 – 10^7 pixels per particle, a metric known as pixel density) and multi-focused, and they capture certain physical properties of the actual particle related to its shape, texture and color. However, during image acquisition and processing, there are uncertainties and errors that affect the quality of the extracted features (see section 1.2.4). These include the effects of (1) the image acquisition and (2) segmentation on the shape, (3) the image resolution, and (4) the focus on the overall of the extracted features.

Effects of image acquisition setting on shape analysis

It is well-known that the results of measurements of the external 3D shape of the particles, from Scanning Electron Microscope (SEM) or optical microscope images, are different from those obtained from 2D cross-sectioned surfaces of the same particles (Liu et al., 2015; Nurfiani and Bouvet de Maisonneuve, 2018; Ross et al., 2022). Such difference is also present in the values of solidity and convexity we obtained, as they are higher than those reported by Liu et al. (2015; Figure 8) who investigated the ash from the same eruption (although not the same exact samples) using different

protocols (Figure 8). Moreover, our solidity and convexity values are also higher than measurements of external 3D particle shapes by Nurfiani and Bouvet de Maisonneuve (2018) using a particle analyzer coupled with an optical microscope system and the same exact samples we used. The possible reasons for such differences are discussed below.

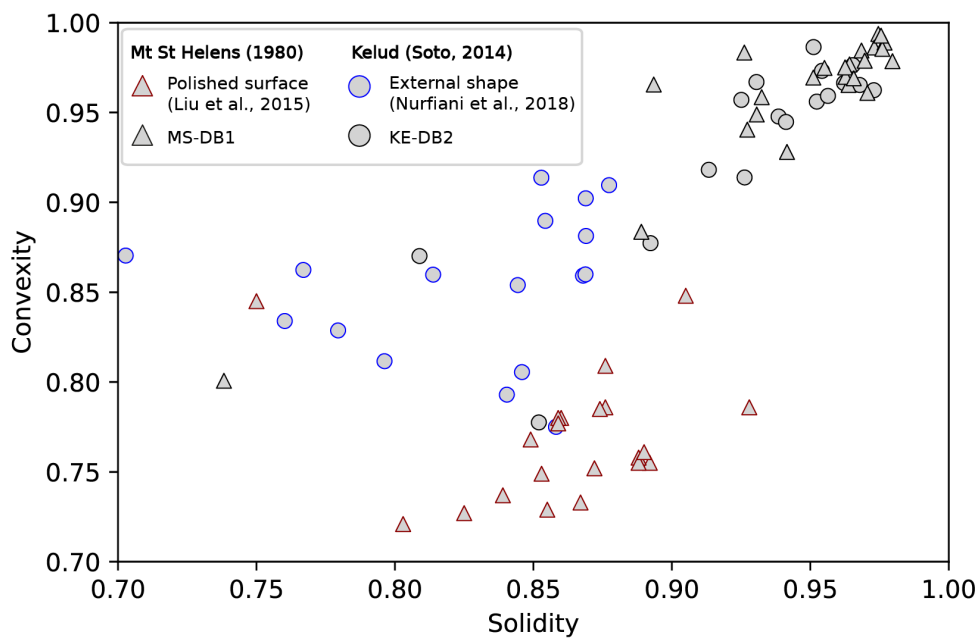


Figure 8: Scatter plot of solidity versus convexity. Our obtained values are much higher than those of Liu et al. (2015), as we use the external shape of a 3D particle to its outline instead of a 2D polished surface. Comparison with external shapes by Nurfiani and Bouvet de Maisonneuve (2018) shows that our values remain higher. We attribute this shift to smoothing of the contours by the segmentation algorithm combined with blurry particle borders.

Effects of image segmentation on shape

Visual inspection of the images with the highest values of solidity and convexity revealed that very small cavities ($<10\mu\text{m}$) present in the original images are absent in the images obtained after segmentation (Figure S3.3). This may have occurred because our original images did not have sufficient resolution, or because the borders of the particle were not sharp enough to allow for fine segmentation by the deep learning model of Qin et al. (2020, see section 1.2.2 for more detail). We compared our values of solidity and convexity of a pumice fragment and a glass shard to those obtained from: (1) SEM images of the 3D external particle shape followed by thresholding (Liu et al., 2015), and (2) the manual refining of the particle shape, e.g., via PhotoShop©, for 2D cross-sectioned particles (e.g., Comida et al., 2022). The convexity values obtained from these techniques are $\sim 25\%$ lower for the pumice fragment, and $\sim 10\%$ lower for the glass shard (Figure 9). On the other hand, the solidity values are very similar suggesting that features sensitive to the particle-scale roughness are not affected. Therefore, it appears that the higher values we obtained for convexity are caused by the smoothing of microscale irregularities upon segmentation, and care should be taken in using these features for potential particle characterization and classification in the future. Improved particle segmentation can be obtained by enhancing the resolution/focus of the original image, by using an improved deep learning algorithm for segmentation of images, or by following either of the

mentioned techniques, although these are time-consuming, and are out of the reach of this study.

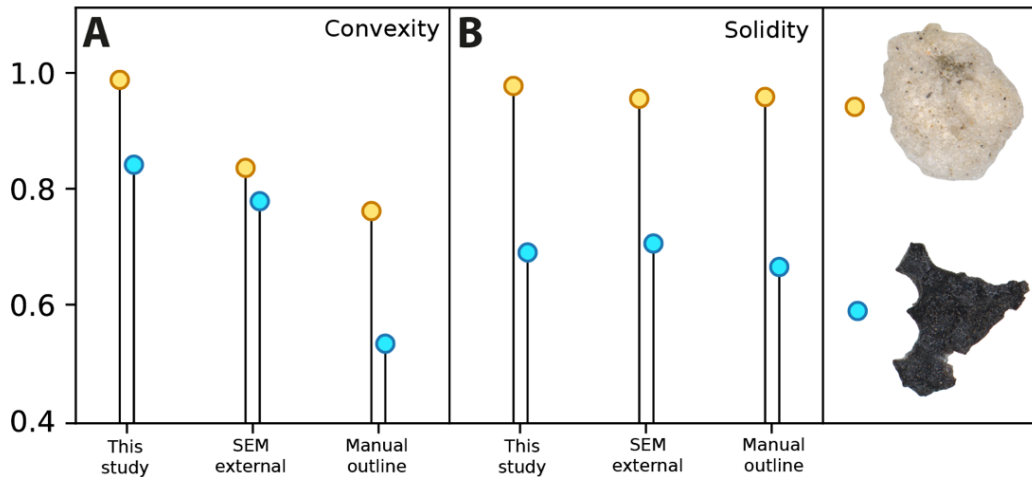


Figure 9: Illustration of the effect of using different segmentation protocols of the retrieved values of (A) convexity, and (B) solidity of a pumice fragment and a glass shard . These include the (1) present study, which uses a deep learning (Qin et al., 2020; see section 1.2.2 for more detail), (2) imaging in the SEM the external shape followed by thresholding to retrieve a binary image, and (3) manually refining the outline by using PhotoShop©. The convexity values for the pumice fragment in this study are much higher than those obtained from the manual outline, as microvesicles were neglected during segmentation. On the other hand, values obtained from the glass shard have more similar values. The solidity values remain stable independently of the method, suggesting that values sensitive to roughness at particle-scale are robust.

Effect of image resolution

To quantify the effect of image resolution and focus on the extracted features, we modeled their response on four particles with distinctive shape, texture, and color: (1) a black, low-crystallinity, fluidal particle from Cumbre Vieja (2021), (2) a pumice fragment and a (3) lithic particle from Kelud (2014), and (4) a hydrothermal aggregate from Soufrière de Guadeloupe (1977). The resolution unit we use to model is defined by the number of pixels comprised in the area of the particle per image (pxls/a), instead of the total number of pixels in the particle image (i.e., pixel density expressed as pxls/p in Liu et al., 2015; Ross et al., 2022), as the latter is affected by the varying distribution of pixels between the background and the particle. The averaged resolution of all our images (6,304) in pixels per particle image is 2.1×10^6 pxls/p, and in pixels per area of the particle is 1.41×10^6 pxls/a. These allow us to estimate the conversion factors between units, i.e., from pxls/a to pxls/p as 1.49, and reversely as 0.67, which we use below. The four particle images we used have a resolution range between 4×10^5 and 4×10^6 pxls/a. The resolution was decreased at steps of 1% (of the order of 10^4 pixels per step) until one step before 0 pxls/a (Figure 10). As the images contain fewer and fewer pixels there is a loss of information including the colors and particle outline in the extracted features. The effect of image resolution on certain color and texture features (*saturation standard deviation* and contrast) starts to change around 3.5×10^4 pxls/a ($\sim 5.22 \times 10^4$ pxls/p), whereas on the shape features, such as solidity, below

1×10^4 pxls/a ($\sim 1.49 \times 10^4$ pxls/p; Figure 10), and thus these are the minimum values that are required.

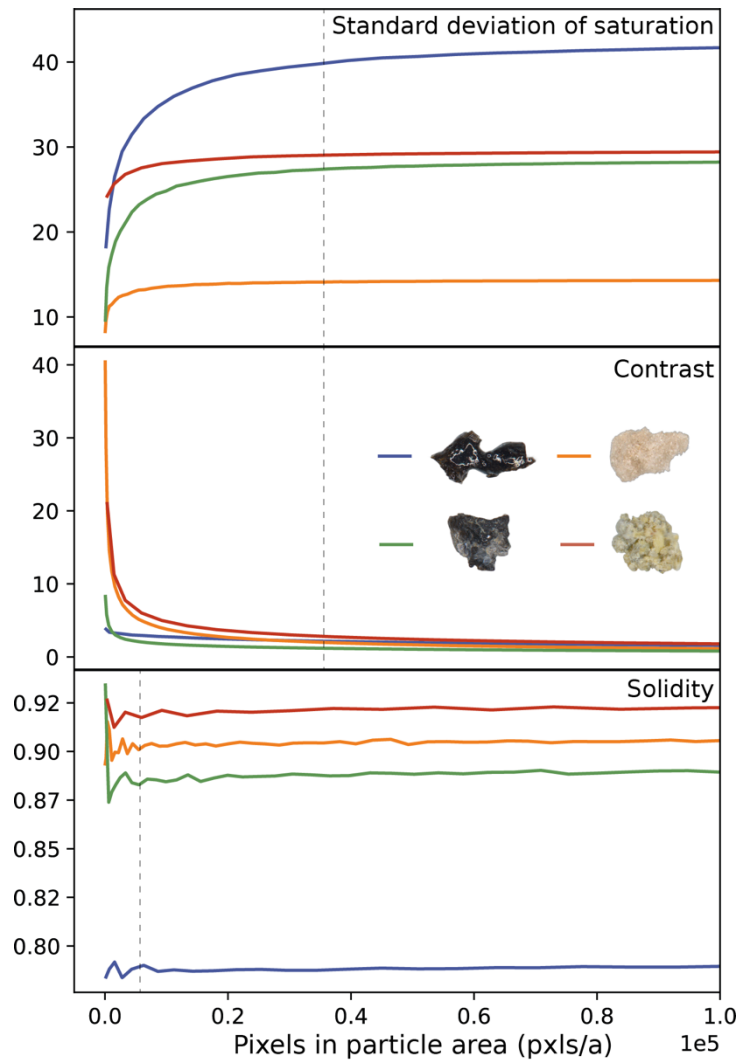


Figure 10: Effect of decreasing the pixels per particle area (pxls/a) on: (A) the standard deviation of the saturation, which measures the variance of intensities within the image, (B) contrast, the repetition rate at which the same pixel values occur in the GLCM (see 'Texture features' in section 1.2.4 for the definition), and (C) solidity, which measures the density. As the resolution decreases, the standard deviation of the saturation decreases exponentially, the contrast increases exponentially, and the solidity becomes more irregular. To obtain robust estimates from our image data type,

a minimum resolution of 3.5×10^4 pxls/a ($\sim 5.22 \times 10^4$ pxls/p) of the particle area is required for proper extraction of texture and color features, whereas 1×10^4 pxls/a ($\sim 1.49 \times 10^4$ pxls/p) for shape features.

Effect of focus

We estimate the overall effect of focus with the image fusion by comparing the distribution of the RGB channels between the multi-focused images and the original single-focus standard binocular images from the same particles. The multi-focused images yielded larger standard deviations, which reflects a wider range of pixel values captured, and thus a better representation of the particle (Figure 11). In addition, we artificially blurred the images of the same test particles using the Scikit-image's function *gaussian blur*. This filter attenuates the high-frequency components of the image, such as the particle outline, giving a translucent appearance (Figure S3.4). With increasing blurriness, the feature extraction was truncated as the particle contrast respect to the background was too low to allow for the particle outline detection. Moreover, the texture features that measure the uniformity of the grayscale, such as homogeneity and correlation, increase linearly with blurriness (Figure S3.4).

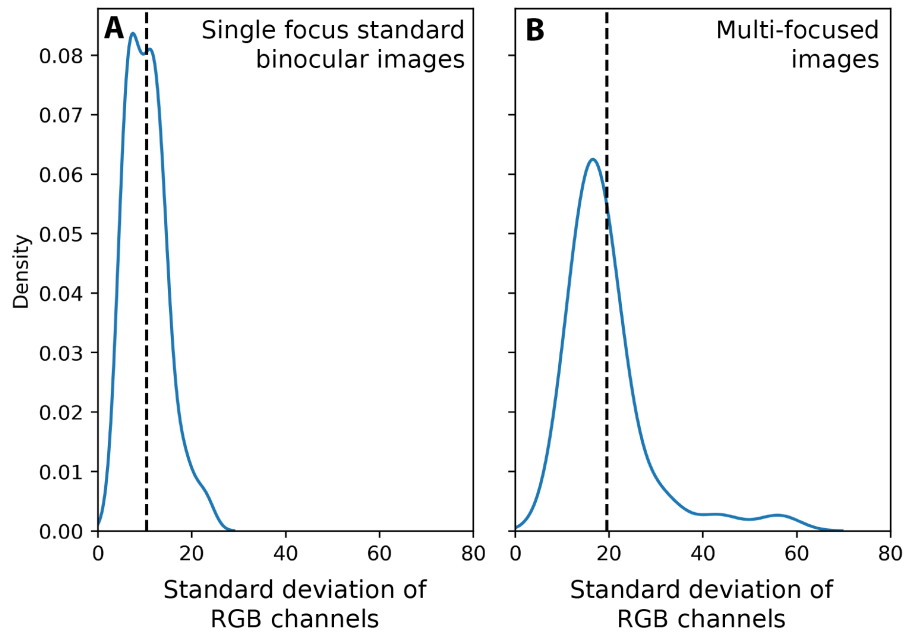


Figure 11: Comparison of the averaged standard deviation of the Red-Green-Blue channels of 34 images taken from the same particles using: (A) unprocessed (standard single focus), and (B) processed (multi-focused) binocular images. The standard deviation is larger for the multi-focused images, as these include a wider variety of pixel intensities given that more parts of the particles are in good focus. The vertical dashed lines indicate the mean of the standard deviation.

1.3 VolcashDB contents

We analyzed 12 samples of volcanic ash from 8 volcanoes and 11 eruptions, and we obtained about 6,304 images of particles that were classified (Table 6). Our collection of ash samples derive from a wide spectrum of volcanic activities:

- (1) Phreatic eruptions: at la Soufrière de Guadeloupe (Lesser Antilles) in 1976 and 1977 (Le Guern et al., 1980; Feuillard et al., 1983), during the early unrest of Mt.

- Pinatubo (Philippines) in April 1991 (Paladio-Melasantos et al., 1996), and from Ontake (Japan) in 2014 (Miyagi et al., 2020);
- (2) Lava dome explosions: at Nevados de Chillán volcanic complex (Chile), from the beginning of the eruptive period in December 2016 and after a dome extrusion in April 2018 (Benet et al., 2021), explosions from Merapi volcano (Indonesia) in July and November 2013 (Nurfiani and Bouvet de Maisonneuve, 2018);
 - (3) Basaltic lava fountaining: at Cumbre Vieja (Canary Islands) in October 2021 (Romero et al., 2022); and
 - (4) Plinian to sub-plinian eruptions: two samples from different locations (KE-DB2 and KE-DB3) of Kelud (Indonesia) in 2014 (Maeno et al., 2019; Utami et al., 2022), and one sample from the main explosive stage of Mount St. Helens (USA) on 8 May 1980 (Scheidegger and Federman, 1983).

Table 6: Main sample characteristics and details, and their proportion of main particle types in number of particles (without normalizing) and associated errors in brackets. The associated error is calculated using equation of margin of error (see section 1.2.7) at a confidence interval of 95% and expressed in absolute values.

Samples	Eruption date	Magma composition	Volcano type	Eruptive style	Number of particles per component and associated error				Total	
					Altered material	Free-crystal	Juvenile	Lithic		
<i>Cumbre Vieja</i>										
CV-DB1	19/10/21	Mafic	Cinder cone	Lava fountaining	3 (± 0.3)	1 (± 0.2)	719 (± 2.8)	352 (± 2.8)	1075	
<i>Kelud</i>										
KE-DB2	14/2/14	Intermediate	Stratovolcano	Subplinian	50 (± 3.9)	4 (± 1.2)	268 (± 4.1)	3 (± 1.0)	325	
KE-DB3	14/2/14	Intermediate	Stratovolcano	Subplinian	162 (± 5.3)	59 (± 4.0)	54 (± 3.9)	65 (± 4.2)	340	
<i>Merapi</i>										
ME-DB1	22/7/13	Intermediate	Stratovolcano	Dome explosion	232 (± 4.9)	13 (± 2.2)	0	78 (± 4.7)	323	
ME-DB2	22/11/13	Intermediate	Stratovolcano	Dome explosion	595 (± 2.9)	76 (± 2.1)	4 (± 0.5)	100 (± 2.4)	775	
<i>Sourfière de Guadeloupe</i>										
SG-DB1	8/7/76	Intermediate	Stratovolcano	Phreatic	222 (± 5.1)	54 (± 3.9)	0	66 (± 4.2)	342	
SG-DB2	1/3/77	Intermediate	Stratovolcano	Phreatic	134 (± 3.8)	8 (± 3.8)	0	0	142	
<i>Nevados de Chillán</i>										
NC-DB15	3/4/18	Intermediate	Dome complex	Dome explosion	224 (± 2.3)	77 (± 1.5)	92 (± 1.6)	749 (± 2.8)	1142	
NC-DB2	29/12/16	Intermediate	Dome complex	Dome explosion	99 (± 5.4)	12 (± 2.3)	14 (± 2.4)	171 (± 5.6)	296	
<i>Ontake</i>										
ON-DB1	27/9/14	Intermediate	Stratovolcano	Phreatic	777 (± 0)	0	0	0	777	
<i>Pinatubo</i>										
PI-DB1	2/4/91	Silicic	Caldera	Phreatic	386 (± 3.7)	104 (± 3.5)	0	16 (± 1.5)	506	
<i>Mount St Helens</i>										
MS-DB1	18/5/80	Silicic	Stratovolcano	Plinian	4 (± 1.5)	0	255 (± 1.8)	2 (± 1.1)	261	
					Total	2888 (± 1.2)	408 (± 0.6)	1406 (± 1.0)	1602 (± 1.0)	6304

The total number of particles per sample vary between about 1100 and 140, and the relative precisions for each particle type varies between a relative error of 53% (2 ± 1.06) for the lithic component of the sample of Mount St Helens down to 0.4% (719 ± 2.81) for the juvenile component of the Cumbre Vieja sample (Table 6). The largest number of particles we classified belongs to the dome eruption of Nevados de Chillán (22%) volcanic complex, whereas samples from each of the other volcanoes represent 10–20% of the total database, except for Mount St Helens which is about 4% (Figure 12A). The most abundant particle type in the database is altered material (47%), followed by juvenile (27%) and lithic (19%) particles, and free crystals (7%; Figure 12B). On a volcano-by-volcano level, the proportions range between two endmembers (Figure 12C): one entirely made of altered material (Ontake, 2014), and the other clearly juvenile-dominated (Mount St. Helens, 1980). The lithic particle content varies from poor (Pinatubo, 1991) to very rich (Nevados de Chillán, 2016–2018).

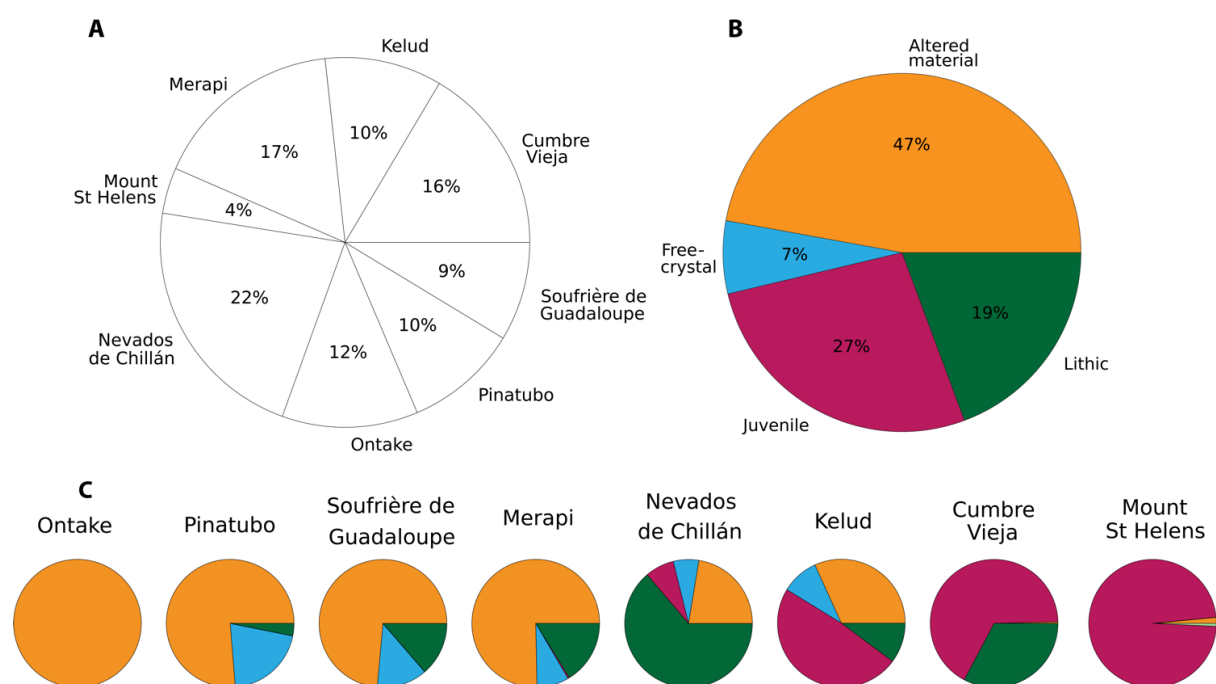


Figure 12: Pie charts showing (A) the percentage of the total number of particles in the database per each volcano, (B) the proportion of the main particle types in the database, and (C) the same as B but per volcano, with particle types show by the colors as in B.

1.3.1 Descriptive of images

The diversity in proportions of particle types reflects the wide range of eruptive styles in our collection. A closer look reveals that ash from samples of the same eruptive style share certain characteristics (Figure 13):

- (1) Ash from the phreatic events (Ontake, 2014; Soufrière de Guadeloupe, 1976–1977; and Pinatubo in the early activity of April 1991) is dominated by altered material (86%), with minor free-crystals and lithics, and contains only accessory amounts (<5%) of juvenile grains. The particles are typically white or red to yellowish, with irregular surfaces, rounded edges, and may form aggregates (Figure 13A). The particle proportions we find are consistent with previous case studies of phreatic activity (e.g., Ontake, 2014, Miyagi et al., 2020; Soufrière de Guadeloupe, Heiken et al., 1980), where the activity has been interpreted to be driven by gas accumulation and interaction with a shallow active hydrothermal system. We don't have samples from low-silica mafic magmas, nor events with interaction with crater lakes.
- (2) Samples from dome explosions in our database (Nevados de Chillán, 2016–2018; Merapi, July and November 2013) are characterized by abundant altered material

(45%) and lithic (43%) grains, with small amounts of free-crystal and juvenile types. Often the particles are coated by hydrothermal material, or they are dark, with massive appearance and high crystallinity (Figure 13B and S5). Samples from dome-forming explosions can vary in juvenile content, from very low (e.g., < 5%, Cashman and Hoblitt, 2004) during precursory activity to high (e.g., > 80%, Benet et al., 2021; Primulyana et al., 2018) as dome extrusion starts.

- (3) The ash particles from lava fountaining (Cumbre Vieja, 2021) contain abundant juvenile grains from fresh magma and also juvenile grains that have been recycled, typically by falling back into the crater (LJ, Figure 13C), and to a lesser extent, lithic and free-crystal types. The juvenile particles are dark, with fluidal to highly vesicular shapes, whereas the recycled juvenile particles (LJ) appear duller and featured by modifications on the surface, such as metallic luster and disseminated red patches. Based on previous experiments and other case studies, the fluidal shape is indicative of magma breakup hydrodynamically (Comida et al., 2022; Gonnermann, 2015), whereas the highly-vesicular particles indicate effective degassing during fragmentation, as for example at Etna (Taddeucci et al., 2002). Particles from this eruptive style have been well documented at Etna (Polacci et al., 2019) and Stromboli (Cannata et al., 2014). We expect that more ash data of this eruptive style will be incorporated in the future either by us or by other users.
- (4) Ash samples we analyzed from a subplinian eruption (Kelud, 2014) contain abundant juvenile particles, and can be recognized by their low-crystallinity and

pumice-like vesiculation (Figure 13D). Moreover, these samples contain variable amounts of lithic and altered material, and minor free-crystals. The presence of pumice-like shape indicates efficient fragmentation due to syn-eruptive volatile expansion and exsolution (Taddeucci and Wohletz, 2001).

- (5) Our ash sample from a plinian eruption (Mount St Helens, 1980) is clearly dominated by the same type of pumice-like juvenile particles (> 95%; Figure 13E) as in subplinian samples. Further grouping of the pumice-like type based on the vesicularity shape and density provide important details of the fragmentation mechanism (Taddeucci and Wohletz, 2001), but it is beyond of the scope of this study. Moreover, studies of the deposits of the opening phase of other plinian eruptions report abundant lithics (e.g., Druitt, 2014), and we expect to add ash samples related to such deposits in the future.

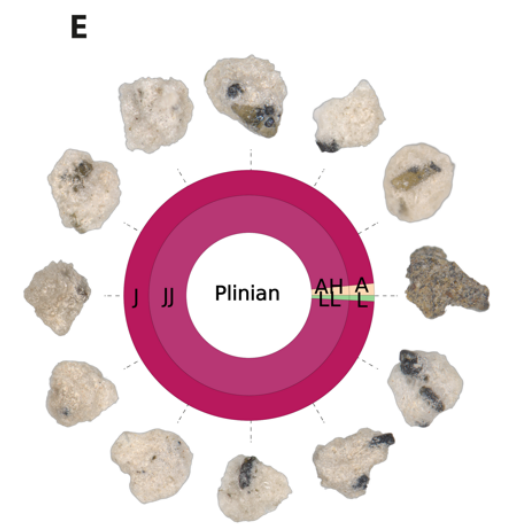
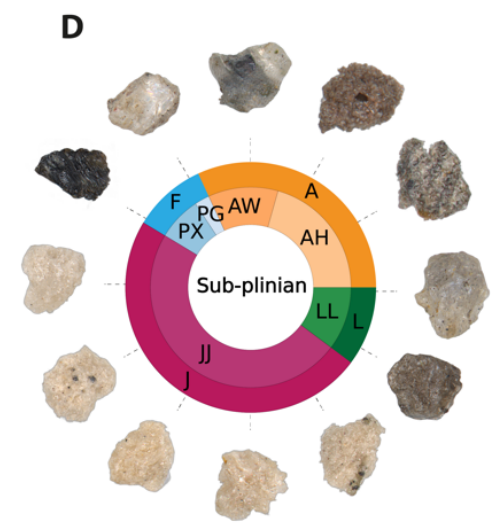
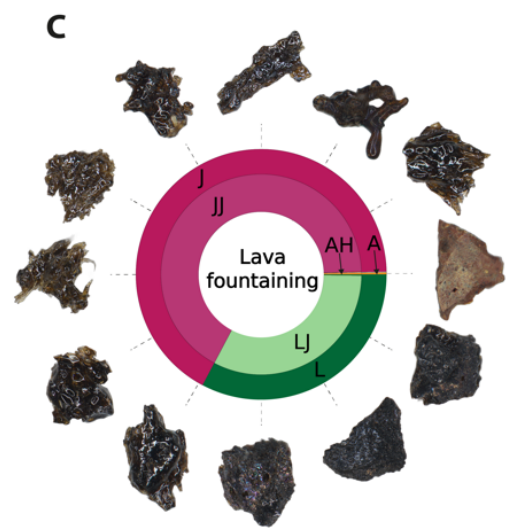
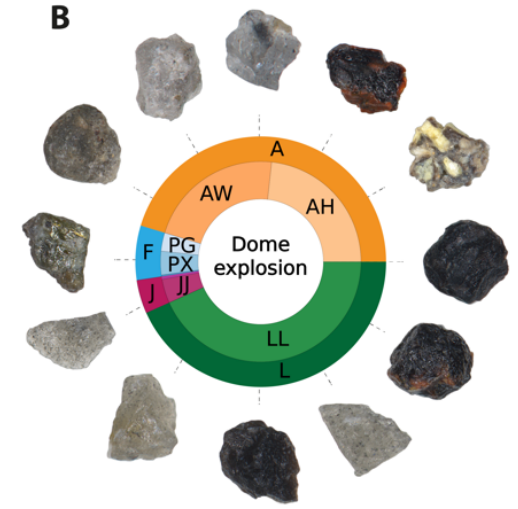
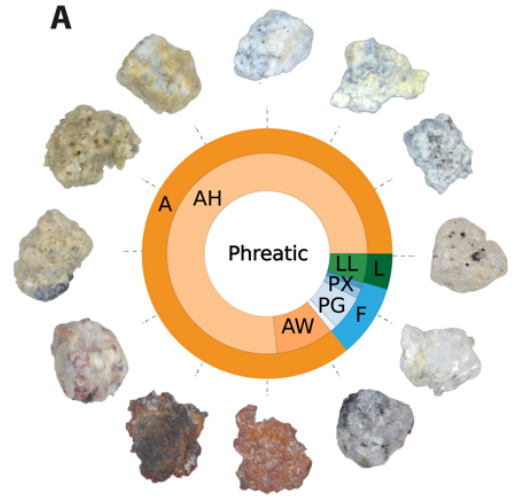


Figure 13: Pie charts showing the proportion of main types and sub-types (Table 4) of particles according to eruptive style. Examples of particle images are shown for the most predominant sub-types per chart. Note the differences in aspect across eruptive styles, e.g., particles from lava fountaining are darker and more elongated, two characteristics that are captured by the Principal Component Analysis (Figure 3.20). Abbreviations as in Table 4: A=Altered material, F=Free-crystal, J=Juvenile, L=Lithic, AH=Hydrothermally altered material, AW=Weathered material, JJ=Standard juvenile, LL=Standard lithic, LJ=Recycled juvenile, PG=Plagioclase, PX=Pyroxene.

1.3.2 Descriptive of features

We extracted a total of 33 features for each particle image which were incorporated in VolcashDB. In this section, we first describe histograms for the different features of the whole database, and then we describe the main particle types and eruptive styles.

Overall feature distributions in the database

Shape and texture features are generally unimodal and their variance ranges widely, from the feature named correlation, which has the lowest variance (Figure 14A), to homogeneity which has the largest (Figure 14B). On the other hand, the color features have very distinct distributions, with wider variance and multimodality, such as the *hue mean* with two modes (Figure 14C), the *red mean* with three (Figure 14D), and four or more for the *blue mode* (Figure 14E) and *value mode*, which has the highest variance (0.27σ ; Figure 14F). Such multimodal distributions with well-defined local maxima

may reflect the different particle types, and thus have more diagnostic power for classification than the low variance features may be less useful for distinguishing between particle types.

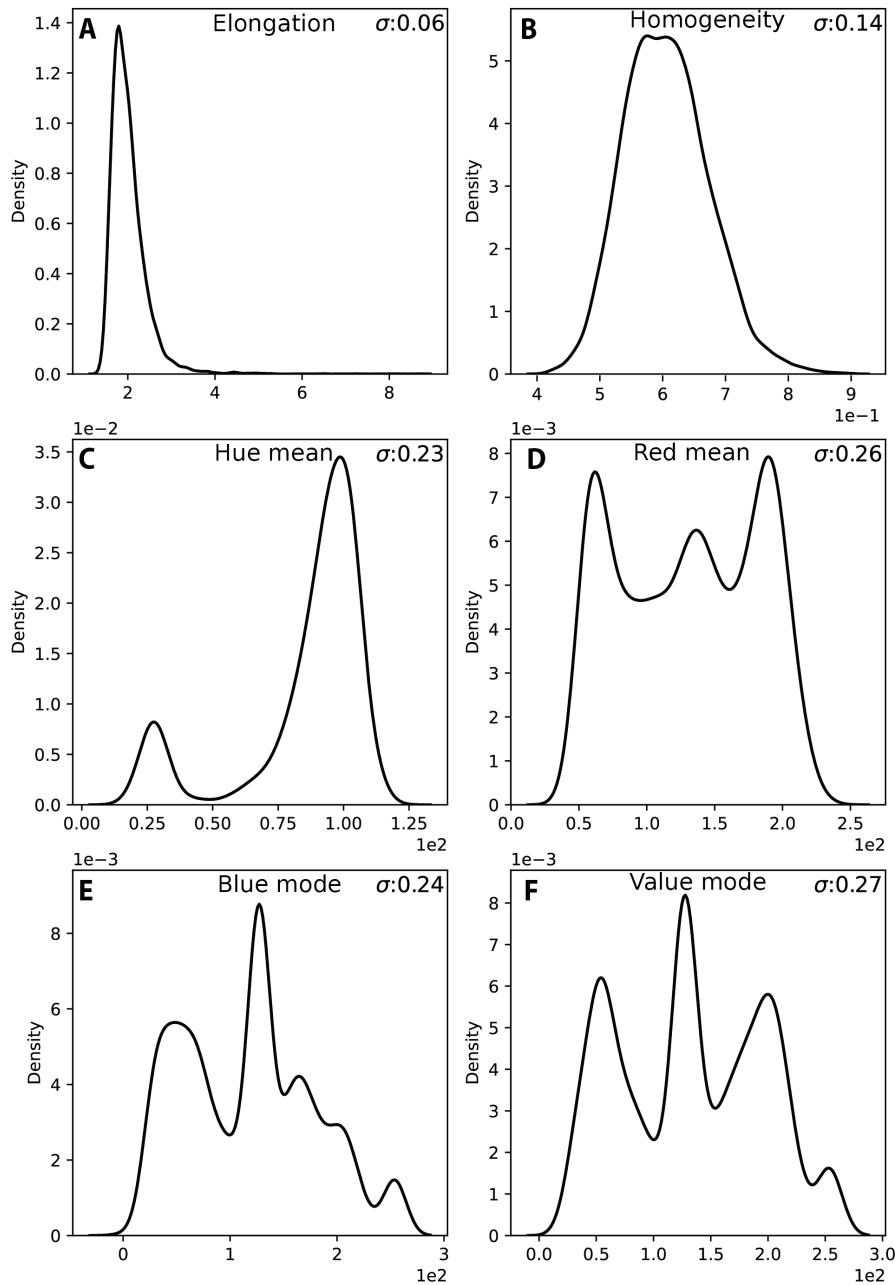


Figure 14: Examples of density plots for six features for all the ash particles in the database. At the top right corner, the standard deviation (σ) is shown and has been calculated after rescaling all features from minimum to max, as 0–1, to allow for

comparison. Shape and texture features are generally unimodal with a range in variance denoted by the narrower elongation (A), and wider homogeneity (B). In contrast, color features show multiple modes and a much wider variance. (C) hue mean shows a bimodal distribution, (D) *red mean* is trimodal, and (E) *blue mode* has multiple modes. (F) the *value mode*, which relates to the intensity or luminance of a particle, has the largest variance of the dataset.

Feature distributions by particle type and eruptive style

The feature histograms were separated into main particle types and eruptive styles to reveal whether certain features can discriminate between one or more of these subgroups. We use the convexity (shape), homogeneity (texture), and value mean (color) to illustrate some of the insights that can be gained.

- (1) The convexity values are similar (mode ~0.98) for the main particle types, except for the juvenile one, which has a somewhat lower values (mode ~0.95 Figure 15A). Filtering by eruptive style reveals that the lower convexity values coincide with particles produced by lava fountaining (Figure 15B). Comparing between main particle types within the lava fountaining style, we identify abundant juvenile particles (Figure 15C) at convexity values < 0.9 , which are the vesicular end of the overall juvenile type (Figure 15A).
- (2) The homogeneity values are similar across particle types, although juvenile particles and free crystals have a greater variance (Figure 15D). The homogeneity values across eruptive styles (Figure 15E) show a slight dispersion of the modes,

from lava fountaining and phreatic (mode ~ 0.55) up to plinian (mode ~ 0.72 ; Figure 15E). The higher values can be explained by the abundance of pumice, which has a similar and uniform appearance under the binocular images, whereas the low values of lava fountaining can be explained by the scattered light reflections observed on the glass shards. The phreatic samples show a low homogeneity group corresponding to altered material (mode ~ 0.55 ; Figure 15F), which possibly consist of the highly heterogeneous material we refer as hydrothermal aggregates and is abundant in the samples Ontake, 2014 and Soufrière de Guadeloupe, 1976–1977. The higher values of homogeneity correspond to free-crystals, typically with crystalline faces, although their variance in the dataset is large (Figure 15D), as they are often adhered to another component.

- (3) The values of the feature *value mean* (from the HSV space), which relates to the intensity of the color, shows three bimodalities and one trimodality for the main particle types (Figure 15G). The bimodality in free-crystals can be explained by the dark (mode ~ 100) and light (\sim mode 220) aspect of the pyroxene and plagioclase. Similarly, the bimodality of lithic particles may respond to the presence of black (mode ~ 60), unaltered lava fragments, typically from dome eruptions, versus lighter (mode ~ 150) modified surfaces. The *value mean* according to eruptive styles separates the previous, juvenile-component bimodality into lava fountaining (mode ~ 70) and plinian (mode ~ 205 ; Figure 15H), and thus a classification threshold could be set between the two around

the value 125. A closer look into the subplinian samples reveals that the juvenile component, with high *value mean* (mode ~200), could be almost fully discriminated from the other components by setting a threshold above 175 (Figure 15I).

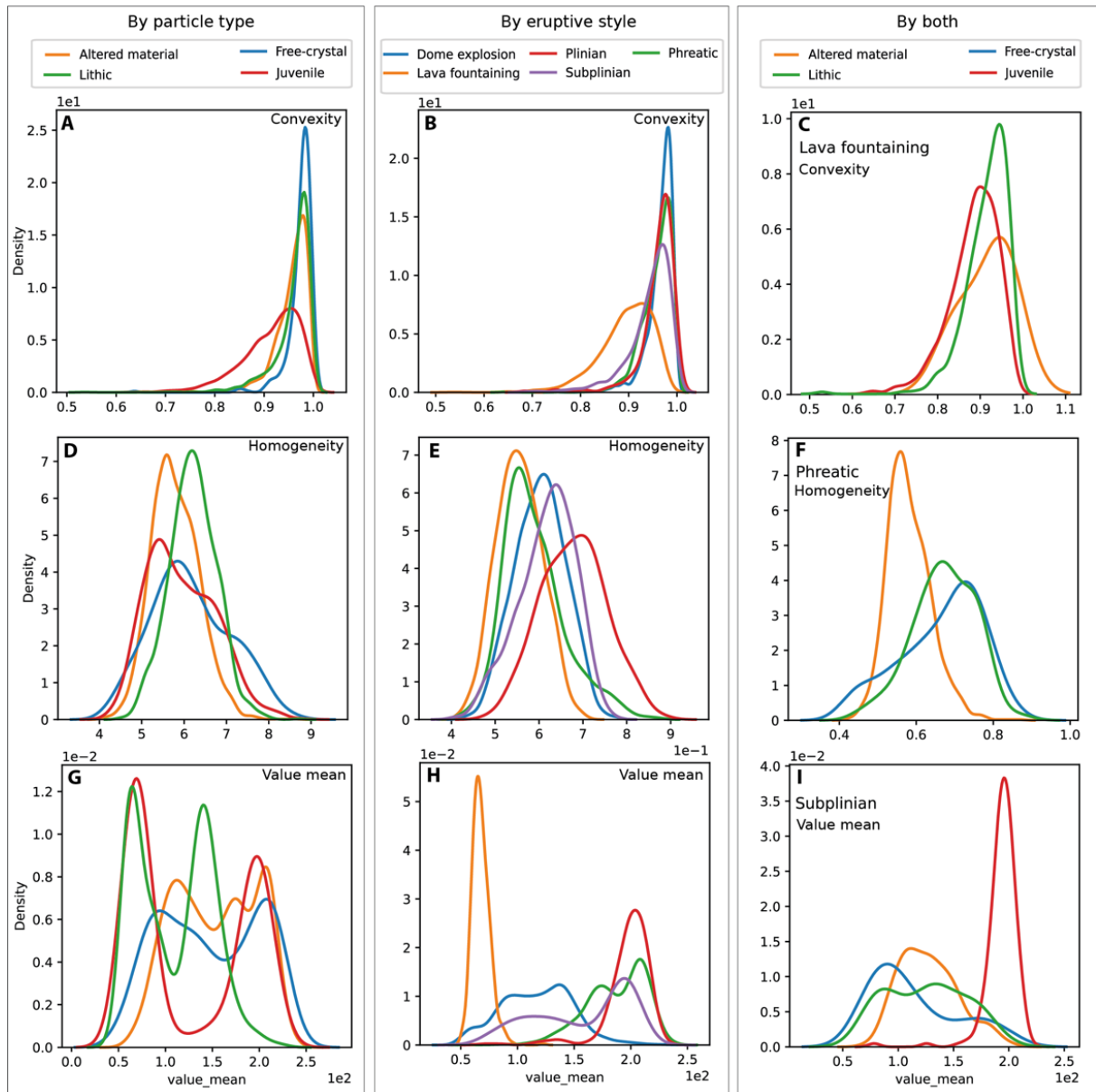


Figure 15: Density plots of convexity (A,B and C), homogeneity (D,E and F) and value mean (G, H and I) across particle types (A, D, G), eruptive styles (B, E, H), and both for a given eruptive style (C, F, I). Note the increase in dispersion of the modes from

top to bottom. While the convexity discriminates slightly one subgroup (A and B), the *value mean* (i.e., mean of the *value* channel of the HSV space) can entirely separate between lava fountaining and plinian (H), and almost isolates juvenile particles for our subplinian samples (I).

1.3.3 VolcashDB Web platform

VolcashDB is an open-access, web-based platform that hosts a curated dataset of the high-resolution, multi-focused images. Each image is linked to its (1) summary label of main the type, sub-type and some of the special characteristics, (2) 33 extracted features, and (3) metadata such as the image magnification, the grain-size or the sample collector. Users can browse through the whole image dataset, or use filters to only visualize particles according to their type, eruptive style, or volcanoes (Figure 16). The platform also contains summary diagrams and plots of the overall proportions in the database and extracted features, as well as their distributions across samples, eruptive styles and volcanoes (Figure 17), which can be selected interactively by the user. Each image is also associated with a file that contains the values of the main extracted features. The images and their related features and classification can be downloaded from the web site in various file formats, after user registration and login at <https://volcash.wovodat.org/database/catalogue>.

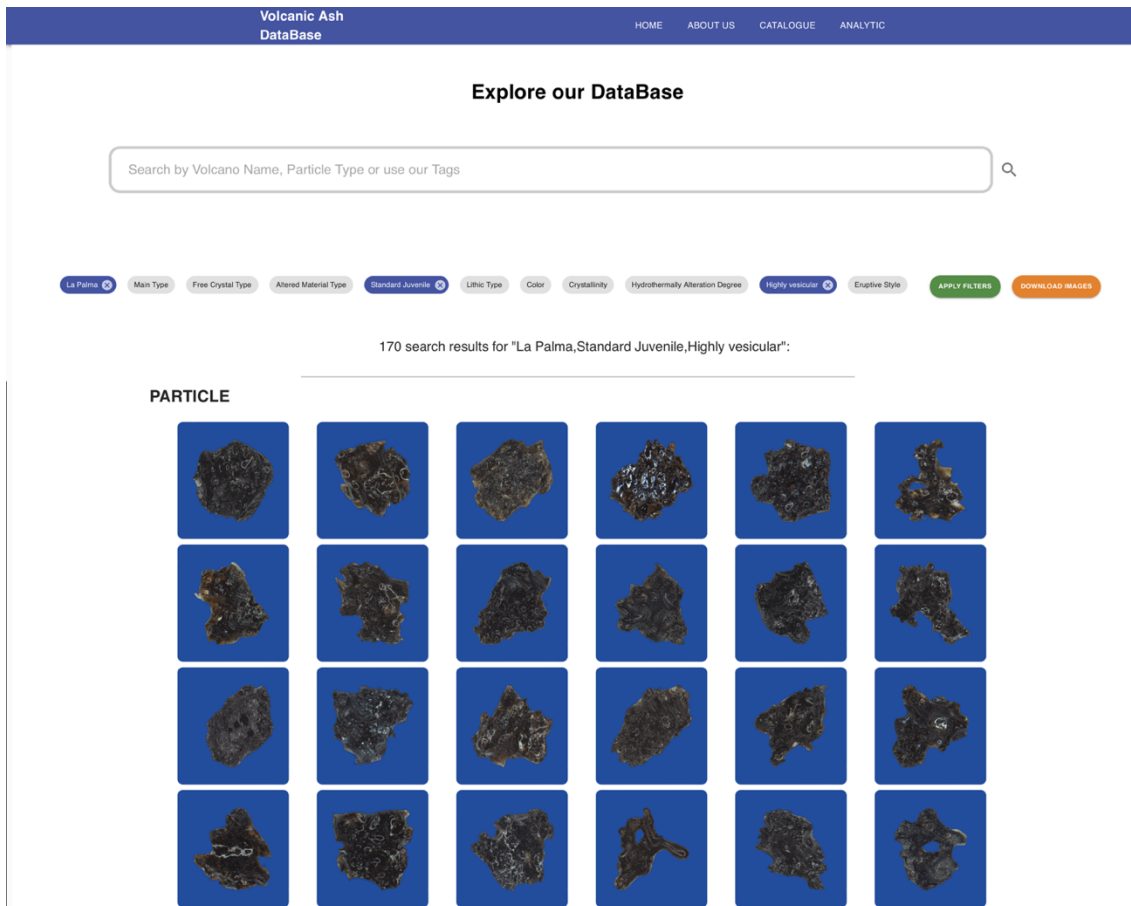


Figure 16: Screen shot of VolcashDB web-based ash image catalogue. The user can search particle images with a combination of tags, by clicking on the scroll down menu of each tag, and 'Apply filters', in green. This selection can be downloaded. In this example, the filters volcano name, juvenile sub-type, and shape are selected to retrieve particles that are from La Palma (Cumbre Vieja), Standard juvenile and Highly vesicular.

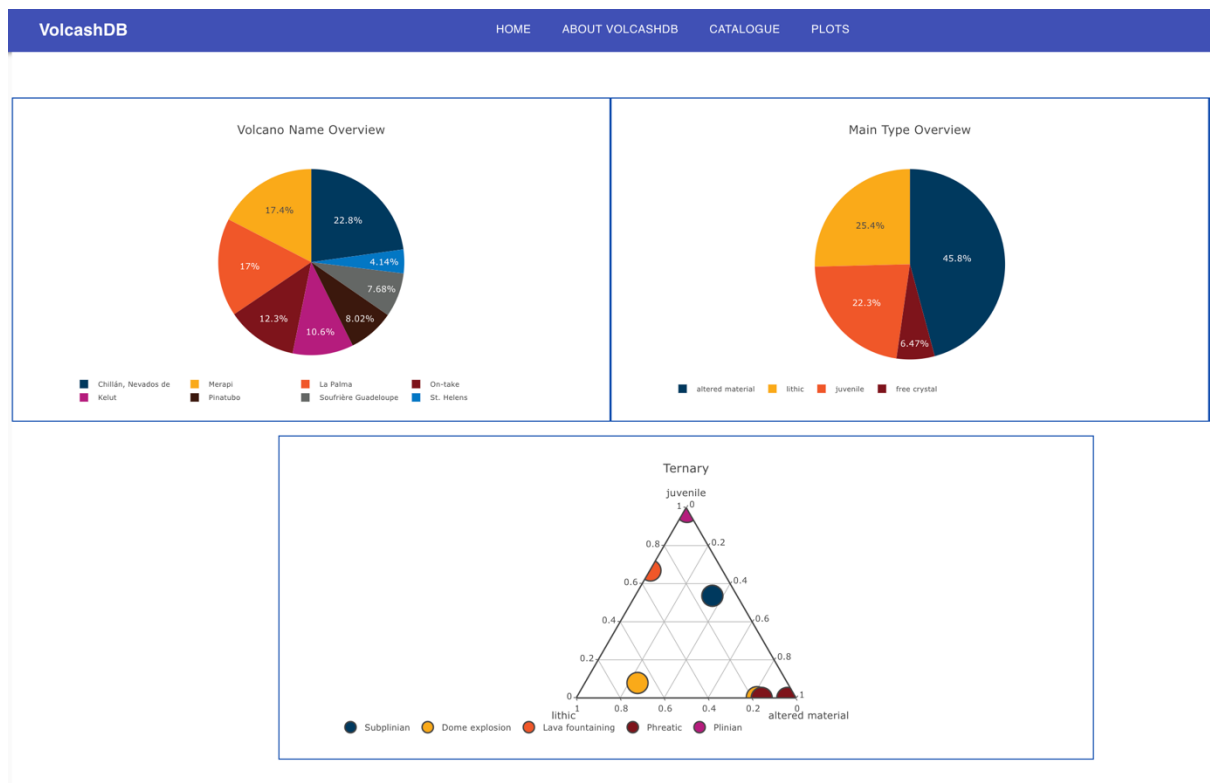


Figure 17: Screen shot of VolcashDB analytics app. Various summary plots and diagrams allow the user to visualize the datasets of classified images and features across eruptive styles and particle types. The plots are interactive, meaning that the user can hover with the mouse to obtain further information, and zoom in and out.

The database content of the platform is stored in a server, using the database manager MongoDB, as it is cost-effective, flexible and can handle many data types (Figure 18). The server infrastructure to receive and process the browser's requests is located under WOVOdat (Newhall et al., 2017), which is a comprehensive global database on volcanic unrest (<https://www.wovodat.org/>). The backend uses several technologies, including JSON, which holds the database, and the open-source libraries Node.js and Flask to execute tasks, such as opening a file on the computer's file system. The

frontend, where the user interacts with the app, uses the open-source JavaScript library React.

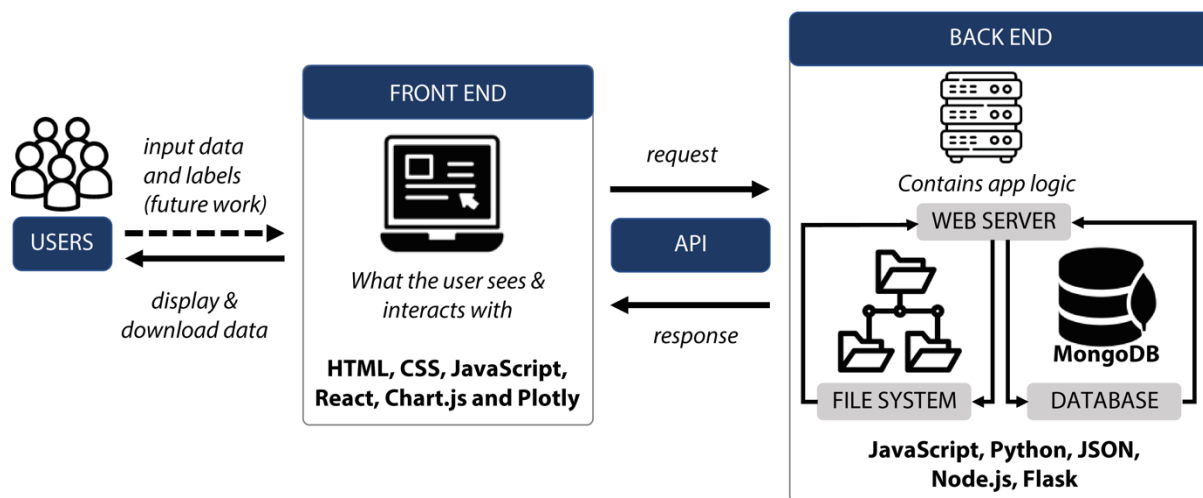


Figure 18: Main components of the web-based platform VolcashDB.

1.4 Discussion

Volcanic eruptions are episodic and of varied nature. Therefore, to be able to anticipate them and understand the processes behind the different eruptive variability we require large multiparametric datasets. Moreover, such data needs to be standardized and curated so that different eruptions and volcanoes can be compared in a robust manner. Data aggregation is the basic of statistical analysis and allows for the calculation of probabilities and the population of event trees of volcanic phenomena (Newhall and Hoblitt, 2002). Several global volcanological databases have been developed over the last decades (Andrews et al., 2022). These include the eruptive records of volcanoes in the Holocene (VOTW; GVP, 2013), the unrest data before, during and after an eruption (WOVOdat; Newhall et al., 2017), the geochemical data of rock and minerals (e.g., EarthChem, GEOROC), geophysical data (e.g., IRIS), and

remote sensing (e.g., ESA Sentinel Online) perhaps being the most complete to date. There currently does not exist a database of volcanic ash particles, although there are some ash image catalogues (e.g., Geological Survey of Japan; https://gbank.gsj.jp/volcano/volcanic_ash/indexe.php). Below we discuss the limitations of the VolcashDB and some examples of possible applications.

1.4.1 Limitations of the current database

VolcashDB contains data about > 6,300 particles from 12 samples and five eruptive styles, for which we obtained the main types and some sub-types proportions, special characteristics, and a list of quantitatively measured features. One limitation is that the petrologic classification of each particle has been conducted by only one observer, and hence the classification is biased, although we strived to use diagnostic observations from the literature as a basis (Fig 6). To improve this in the future, classification should result from the aggregated knowledge and experience of various experts in the field. This could be accomplished via workshops and publications where several researchers classify the same particles and using expert elicitation (Aspinall and Blong, 2015) would allow to treat the problem in probabilistic terms. This approach has been successfully done in other volcanological studies dealing with highly uncertain situations. A related limitation is that each particle belongs 100% to a given type, which implies 100% certainty of the class to which this particle belongs. A more robust classification could include a percentage of a given particle to belong to a given class without these being mutually exclusive. For instance, if a particle

exhibits four out of five fresh-like features, and the weights are equally distributed, the particle could be assigned 80% of probability of being juvenile. Other limitations of the database are the range of eruptive styles and magma compositions. We currently have not yet incorporated ash particles from vulcanian or strombolian eruptions, or from phreatomagmatic events driven by water-magma interactions. In terms of magma compositions, we are also lacking andesites. A future goal of the database is to make it more complete by incorporating data from our own samples, but also to make the platform open for any user to upload ash image samples that would be classified into the different types so that the database could grow by the community as it is the case for WOVOdat (Costa et al., 2019).

1.4.2 Applications in comparative studies

The ash particle images and characteristics that we have compiled could be used to compare with other ash particles in a visual manner, and thus may help to decide users to which category belongs a given particle from a given volcano and eruption they are studying. Moreover, external datasets could be imported to VolcashDB to examine their relationship qualitatively (e.g., plots) or quantitatively by using statistical tools (e.g., dendrograms, amongst others in Dürig et al., 2021), if such datasets are comparable based on the followed methodological protocols and statistical tests (Dürig et al., 2021).

Our results show that the ash samples from different volcanoes and eruptive styles have distinctive particle proportions and features. This means that we can compare between samples and quantify their similarity at a specific variable. A manner in which one could compare between eruptions using ash is to use the proportions of the main particle types and visualize them using a ternary diagram of the juvenile, altered material, and lithic (Figure 19). Such ternary diagram shows that samples from activity that does not directly involve magma (phreatic) or only to a limited extent (dome explosions) plot closer (along the isoline of 0% of juvenile content), than those from lava fountaining, subplinian, and plinian samples (between the isolines 20-100% of juvenile content). Adding more samples, including Strombolian and Vulcanian eruptive styles, and using additional features, such as the particles shape, texture and color, statistical clustering could be used to quantify their similarity in the context of analogue volcanoes. Users could plot the proportions of the ash samples that they are studying and compare with the eruptions we have produced in the database. It should be also possible to plot a time series of ash samples that visually shows how the volcano may be going from a mainly phreatic phase towards a magmatic eruption (e.g., Suzuki et al., 2013).

straightforward statistical tool to gain an understanding of the underlying data structure and compare between samples and particles is using Principal Component Analysis (PCA). In PCA, new variables are constructed as linear combination of the original variables (here referred as features) while retaining as much variance as possible (Smith, 2002). PCA has been extensively used for dimension reduction of shape features in volcanic ash and has allowed for instance to identify different morphological types of particles.

We applied PCA to the juvenile particles to investigate their data structure and which features contribute the most to the variance. We first undersampled juvenile particles by eruptive styles to obtain a balanced dataset, and standardized the features using Scikit-Learn's *standard scaler*. Dimensionality was reduced by defining 10 new variables, hereafter referred as principal components, by eigen decomposition (the reader is referred to Dürig et al., 2021 for a step-by-step explanation on this method), which can be implemented from the Python package *pca* (<https://erdogant.github.io/pca/>).

The 10 obtained principal components (PC) retained 95% of the variance of the original dataset, 50% and 14% of which correspond to the first (PC1) and second (PC2) components (Figure 20A). The distribution of the PC1 versus PC2 across eruptive styles reveals two main clusters, one around -4 in PC1, where plinian and subplinian juvenile particles coexist, and a second around +6 in PC1, consisting almost entirely of

lava fountaining shards. In between the two, there is a less defined group of juvenile particles from dome explosions. The most contributing features to PC1 are related to the color and is led by the *green mode* with a contribution to variance of -0.2 (Table S3.1), whereas elongation is the main contributor (+0.3) to PC2 (Figure 20B). In summary, up to 65% (added variance of PC1 and PC2) of the total variance of the dataset can be explained mainly by the PC1, which results from a linear combination of color features, and roughly separates eruptive styles into clusters. This example shows that color features can proportionate a wealth of information critical for discrimination, consistently with previous research (Miwa et al., 2015; Yamanoi et al., 2008), and thus that data from binocular imaging systems can help characterize volcanic ash particles in a robust manner.

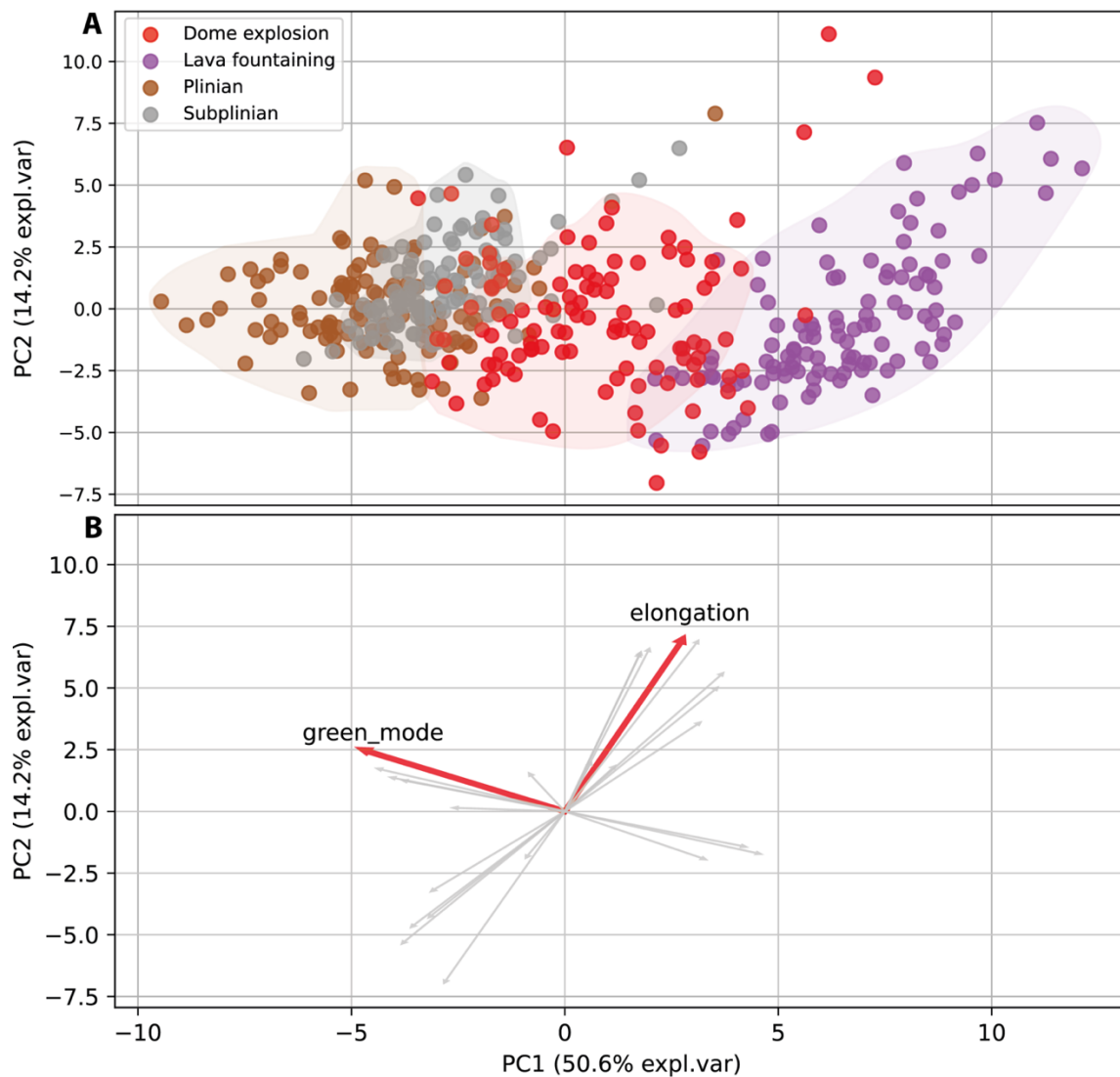


Figure 20: (A) Scatter plot of the first (PC1) and second (PC2) principal components, which are extracted from our feature dataset, for juvenile particles. The contribution of each component to explain the variance of the original dataset is shown in brackets. The spread of the particles by eruptive style shows two distinct clusters, a subplinian and plinian, and another of lava fountaining, with the dome explosion in between. (B) Representation of the contribution of the features as arrows, with emphasis on the main contributors (in red) to interpret the PC1 and PC2. The arrow angle indicates the contribution of the feature in the direction of the component where it contributes,

whereas the length indicates the strength of the contribution. The `green_mode` is the largest contributor to the PC1, followed by other color features (Table S3.1), whereas elongation is the largest contributor to the PC2, along with other shape features (Table S3.1).

1.4.4 Applications for automatic classification and machine learning

The images and characteristics of particles we have compiled could also be used to train machine learning models. This would allow to move towards automatic particle classification that would be standardized and in principle independent of the observer, and thus the ash componentry between different eruptions can be compared in an objective and reproducible manner. Object classification via image observations is a problem that could be addressed by applying machine learning (ML). ML includes a series of techniques that allow models to learn from data with minimum human intervention. ML has been already applied for classification in several fields, e.g., plants based on their leaves (Aakif and Khan, 2015), variable stars (Hosenie et al., 2019), and also in volcanic ash for classifying into their shapes (Shoji et al., 2018). These often require a large amount of standardized and widely representative data about particle features, images, or even chemical composition and the database that we have started could be the basis for such an endeavor.

1.5 Conclusions

Volcanic ash provides critical insights to the state of a volcano, but its use requires classifying the particles into types and there is no standardized methodology to do so and diagnostic observations depend on the eruptive style. In this contribution we developed a standardized methodology to obtain high-quality images of a relatively large number of particles, extracted up to 33 features from the images, and classified the particles following the diagnostic observations from previous studies in the literature. We obtained a dataset includes 6,304 ash particles from a range of eruptive styles which we used to create VolcashDB, a public web-based platform that allows users to browse and download various data types. We believe such platform and dataset should be useful in comparative studies and the basis for Machine Learning algorithms towards an automated and unbiased ash particle classification.

Acknowledgements

I am very grateful to Charles Tran, Khai Truong and Bui Quang for their invaluable help on the development of the VolcashDB web-app and the MongoDB collection, to Edwin Tan for support on the Gekko cluster, to Vanesa Burgos for help on the PCA analysis, and to Caroline Bouvet de Maisonneuve for insightful discussions. This research was supported by the Earth Observatory of Singapore via its funding from the National Research Foundation Singapore and the Singapore Ministry of Education under the Research Centres of Excellence initiative.

References

- Aakif, A., Khan, M.F., 2015. Automatic classification of plants based on their leaves. *Biosyst. Eng.* 139, 66–75. <https://doi.org/10.1016/j.biosystemseng.2015.08.003>
- Aiuppa, A., 2015. Volcanic gas monitoring. A. Schmidt, K.E. Fristad, L.T. Elkins-Tanton (Eds.), *Volcanism and Global Environmental Change*, Cambridge University Press (2015), pp. 81-96.
- Alvarado, G.E., Mele, D., Dellino, P., de Moor, J.M., Avard, G., 2016. Are the ashes from the latest eruptions (2010–2016) at Turrialba volcano (Costa Rica) related to phreatic or phreatomagmatic events? *J. Volcanol. Geotherm. Res.* 327, 407–415. <https://doi.org/10.1016/j.jvolgeores.2016.09.003>
- Andrews, B.J., Costa, F., Venzke, E., Widiwijayanti, C., 2022. Databases in *Volcanology. Bull. Volcanol.* 84, 1–6. <https://doi.org/10.1007/s00445-022-01597-x>
- Aspinall, W., Blong, R., 2015. *Volcanic Risk Assessment, Second Edition*, The Encyclopedia of Volcanoes. Elsevier Inc. <https://doi.org/10.1016/B978-0-12-385938-9.00070-5>
- Aspinall, W., Cooke, R.M., 1998. Expert Judgement and the Montserrat Volcano Eruption. *Proceeding 4th Int. Conf. Probabilistic Saf. Assess. Manag. PSAM4* 3, 2113–2118.
- Bebbington, M.S., Jenkins, S.F., 2019. Intra-eruption forecasting.
- Benet, D., Costa, F., Pedreros, G., Cardona, C., 2021. The volcanic ash record of shallow magma intrusion and dome emplacement at Nevados de Chillán

Volcanic complex, Chile. *J. Volcanol. Geotherm. Res.* 417.

<https://doi.org/10.1016/j.jvolgeores.2021.107308>

Cannata, C.B., Rosa, R. De, Donato, P., Taddeucci, J., 2014. Ash Features from Ordinary Activity at Stromboli Volcano. *Int. J. Geosci.* 05, 1361–1382.

<https://doi.org/10.4236/ijg.2014.511111>

Cashman, K. V., Hoblitt, R.P., 2004. Magmatic precursors to the 18 May 1980 eruption of Mount St. Helens, USA. *Geology* 32, 141–144.

<https://doi.org/10.1130/G20078.1>

Chouet, B., 2003. Volcano seismology. *Pure Appl. Geophys.* 160, 739–788.

<https://doi.org/10.1007/PL00012556>

Cioni, R., Pistolesi, M., Bertagnini, A., Bonadonna, C., Hoskuldsson, A., Scatani, B., 2014. Insights into the dynamics and evolution of the 2010 Eyjafjallajökull summit eruption (Iceland) provided by volcanic ash textures. *Earth Planet. Sci. Lett.* 394, 111–123. <https://doi.org/10.1016/j.epsl.2014.02.051>

Comida, P.P., Ross, P.S., Dürig, T., White, J.D.L., Lefebvre, N., 2022. Standardized analysis of juvenile pyroclasts in comparative studies of primary magma fragmentation: 2. Choice of size fraction and method optimization for particle cross-sections. *Bull. Volcanol.* 84, 1–24. <https://doi.org/10.1007/s00445-021-01517-5>

5

Costa, F., Widiwijayanti, C., Nang, T.Z.W., Fajiculay, E., Espinosa-Ortega, T.,

Newhall, C., 2019. WOVOdat – the global volcano unrest database aimed at

improving eruption forecasts. *Disaster Prev. Manag. An Int. J.* 28, 738–751.

<https://doi.org/10.1108/DPM-09-2019-0301>

D’Oriano, C., Bertagnini, A., Cioni, R., Pompilio, M., 2014. Identifying recycled ash in basaltic eruptions. *Sci. Rep.* 4. <https://doi.org/10.1038/srep05851>

Dellino, P., La Volpe, L., 1996. Image processing analysis in reconstructing fragmentation and transportation mechanisms of pyroclastic deposits. The case of Monte Pilato-Rocche Rosse eruptions, Lipari (Aeolian islands, Italy). *J. Volcanol. Geotherm. Res.* 71, 13–29. [https://doi.org/10.1016/0377-0273\(95\)00062-3](https://doi.org/10.1016/0377-0273(95)00062-3)

Doyle, E.E.H., McClure, J., Paton, D., Johnston, D.M., 2014. Uncertainty and decision making: Volcanic crisis scenarios. *Int. J. Disaster Risk Reduct.* 10, 75–101. <https://doi.org/10.1016/j.ijdr.2014.07.006>

Druitt, T.H., 2014. New insights into the initiation and venting of the Bronze-Age eruption of Santorini (Greece), from component analysis. *Bull. Volcanol.* 76, 1–21. <https://doi.org/10.1007/s00445-014-0794-x>

Dürig, T., Bowman, M.H., White, J.D.L., Murch, A., Mele, D., Verolino, A., Dellino, P., 2018. Particle shape analyzer Partisan - An open source tool for multi-standard two-dimensional particle morphometry analysis. *Ann. Geophys.* 61. <https://doi.org/10.4401/ag-7865>

Dzurisin, D., 2006. *Volcano deformation: new geodetic monitoring techniques.* Springer Science & Business Media.

Gaunt, H.E., Bernard, B., Hidalgo, S., Proaño, A., Wright, H., Mothes, P., Criollo, E., Kueppers, U., 2016. Juvenile magma recognition and eruptive dynamics inferred

from the analysis of ash time series: The 2015 reawakening of Cotopaxi volcano.

J. Volcanol. Geotherm. Res. 328, 134–146.

<https://doi.org/10.1016/j.jvolgeores.2016.10.013>

Global Volcanism Program, 2013. Volcanoes of the World, v. 4.11.2 (02 Sep 2022).

Venzke, E (ed.). Smithsonian Institution. Downloaded 13 Sep 2022.

<https://doi.org/10.5479/si.GVP.VOTW4-2013>.

Gonnermann, H.M., 2015. Magma Fragmentation. Annu. Rev. Earth Planet. Sci. 43,

431–458. <https://doi.org/10.1146/annurev-earth-060614-105206>

Gunawan, H., Surono, Budianto, A., Kristianto, Prambada, O., McCausland, W.,

Pallister, J., Iguchi, M., 2019. Overview of the eruptions of Sinabung Volcano,

2010 and 2013–present and details of the 2013 phreatomagmatic phase. J.

Volcanol. Geotherm. Res. 382, 103–119.

<https://doi.org/10.1016/j.jvolgeores.2017.08.005>

Hall-Beyer, M., 2017. GLCM Texture: A Tutorial. 17th Int. Symp. Ballist. 2, 18–19.

Haralick, R.M., Dinstein, I., Shanmugam, K., 1973. Textural Features for Image

Classification. IEEE Trans. Syst. Man Cybern. SMC-3, 610–621.

<https://doi.org/10.1109/TSMC.1973.4309314>

He, K., Zhang, X., Ren, S., Sun, J., 2015. Delving deep into rectifiers: Surpassing

human-level performance on imagenet classification. Proc. IEEE Int. Conf.

Comput. Vis. 1026–1034.

- Heiken, G., Crowe, B., McGetchin, T., West, F., Eichelberger, J., Bartram, D., Peterson, R., Wohletz, K., 1980. Phreatic Eruption Clouds: the Activity of La Soufrière de Guadeloupe. *Bull. Volcanol.* 43.
- Heiken, G., Wohletz, K., 1985. *Volcanic Ash*. University Presses of California, Chicago, Harvard & MIT.
- Hincks, T.K., Komorowski, J.C., Sparks, S.R., Aspinall, W.P., 2014. Retrospective analysis of uncertain eruption precursors at La Soufrière volcano, Guadeloupe, 1975-77: Volcanic hazard assessment using a Bayesian Belief Network approach. *J. Appl. Volcanol.* 3. <https://doi.org/10.1186/2191-5040-3-3>
- Hosenie, Z., Lyon, R.J., Stappers, B.W., Mootoovaloo, A., 2019. Comparing multiclass, binary, and hierarchical machine learning classification schemes for variable stars. *Mon. Not. R. Astron. Soc.* 488, 4858–4872. <https://doi.org/10.1093/mnras/stz1999>
- Houghton, B.F. and Smith, R.T., 1993. Recycling of magmatic clasts during explosive eruptions: estimating the true juvenile content of phreatomagmatic volcanic deposits. *Bulletin of volcanology*, 55(6), pp.414-420.
- Hughes, Ifan G., Hase, T.P.A., 2010. Uncertainties in single-variable.
- Ibraheem, N. a, Hasan, M.M., Khan, R.Z., Mishra, P.K., 2012. Understanding Color Models : A Review. *ARNP J. Sci. Technol.* 2, 265–275.
- Le Guern, F., Bernard, A., Chevrier, R.M., 1980. Soufrière of Guadeloupe 1976–1977 eruption –mass and energy transfer and volcanic health hazards. *Bull. Volcanol.* 43, 577–593. <https://doi.org/10.1007/BF02597694>

- Leibbrandt, S., Le Pennec, J.L., 2015. Towards fast and routine analyses of volcanic ash morphometry for eruption surveillance applications. *J. Volcanol. Geotherm. Res.* 297, 11–27. <https://doi.org/10.1016/j.jvolgeores.2015.03.014>
- Li, L., Iskander, M., 2022. Use of machine learning for classification of sand particles. *Acta Geotech.* 0123456789. <https://doi.org/10.1007/s11440-021-01443-y>
- Liu, E.J., Cashman, K. V., Rust, A.C., 2015. Optimising shape analysis to quantify volcanic ash morphology. *GeoResJ* 8, 14–30. <https://doi.org/10.1016/j.grj.2015.09.001>
- Loughlin, S.C., Sparks, S., Brown, S.K., Jenkins, S.F., Vye-Brown, C., (Eds.), 2015. *Global volcanic hazard and risk*, Cambridge. ed, *Global Volcanic Hazards and Risk*. <https://doi.org/10.1017/CBO9781316276273>
- Ma, B., Zhu, Y., Yin, X., Ban, X., Huang, H., Mukeshimana, M., 2021. SESF-Fuse: an unsupervised deep model for multi-focus image fusion. *Neural Comput. Appl.* 33, 5793–5804. <https://doi.org/10.1007/s00521-020-05358-9>
- Maeno, F., Nakada, S., Yoshimoto, M., Shimano, T., Hokanishi, N., Zaennudin, A., Iguchi, M., 2019. A sequence of a plinian eruption preceded by dome destruction at Kelud volcano, Indonesia, on February 13, 2014, revealed from tephra fallout and pyroclastic density current deposits. *J. Volcanol. Geotherm. Res.* 382, 24–41. <https://doi.org/10.1016/j.jvolgeores.2017.03.002>
- Maitre, J., Bouchard, K., Bédard, L.P., 2019. Mineral grains recognition using computer vision and machine learning. *Comput. Geosci.* 130, 84–93. <https://doi.org/10.1016/j.cageo.2019.05.009>

- Marzocchi, W., Bebbington, M.S., 2012. Probabilistic eruption forecasting at short and long time scales. *Bull. Volcanol.* 74, 1777–1805.
<https://doi.org/10.1007/s00445-012-0633-x>
- Mendenhall, W., Beaver, R.J. and Beaver, B.M., 2012. Introduction to probability and statistics. Cengage Learning.
- Minami, Y., Imura, T., Hayashi, S., Ohba, T., 2016. Mineralogical study on volcanic ash of the eruption on September 27, 2014 at Ontake volcano, central Japan: Correlation with porphyry copper systems the Phreatic Eruption of Mt. Ontake Volcano in 2014 5. *Volcanology. Earth, Planets Sp.* 68.
<https://doi.org/10.1186/s40623-016-0440-2>
- Miwa, T., Geshi, N., Shinohara, H., 2013. Temporal variation in volcanic ash texture during a vulcanian eruption at the Sakurajima volcano, Japan. *J. Volcanol. Geotherm. Res.* 260, 80–89. <https://doi.org/10.1016/j.jvolgeores.2013.05.010>
- Miwa, T., Shimano, T., Nishimura, T., 2015. Characterization of the luminance and shape of ash particles at Sakurajima volcano, Japan, using CCD camera images. *Bull. Volcanol.* 77. <https://doi.org/10.1007/s00445-014-0886-7>
- Miyagi, I., Geshi, N., Hamasaki, S., Oikawa, T., Tomiya, A., 2020. Heat source of the 2014 phreatic eruption of Mount Ontake, Japan. *Bull. Volcanol.* 82.
<https://doi.org/10.1007/s00445-020-1358-x>
- Muller, G. 1967. Methods in sedimentary petrology. Section in: Degree of roundness according to Russel-Taylor-Pettijohn (after Schneiderhohn) New York, Hafner Publishing Company. 100-101.

- Newhall, C., Hoblitt, R., 2002. Constructing event trees for volcanic crises. *Bull. Volcanol.* 64, 3–20. <https://doi.org/10.1007/s004450100173>
- Newhall, C.G., Costa, F., Ratdomopurbo, A., Venezky, D.Y., Widiwijayanti, C., Win, N.T.Z., Tan, K., Fajiculay, E., 2017. WOVOdat – An online, growing library of worldwide volcanic unrest. *J. Volcanol. Geotherm. Res.* 345, 184–199. <https://doi.org/10.1016/j.jvolgeores.2017.08.003>
- Newhall C.G., Punongbayan R.S., 1996. The narrow margin of successful volcanic-risk mitigation. In: Scarpa, R., Tilling, R.I., editors. *Monitoring and mitigation of volcanic hazards*. Berlin Heidelberg: Springer Verlag; 1996, pp.807–38.
- Nurfiani, D., Bouvet de Maisonneuve, C., 2018. Furthering the investigation of eruption styles through quantitative shape analyses of volcanic ash particles. *J. Volcanol. Geotherm. Res.* 354, 102–114. <https://doi.org/10.1016/j.jvolgeores.2017.12.001>
- Paladio-Melasantos, M.L., Solidum, R.U., Scott, W.E., Quiambao, R.B., Umbal, J. V, Rodolfo, K.S., Tubianosa, B.S., Delos Reyes, P.J., Alonso, R.A., Ruerlo, H.B., 1996. Tephra falls of the 1991 eruptions of Mount Pinatubo. Newhall, C.G. others, *Fire mud; eruptions lahars Mt. Pinatubo, Philipp.* Philipp. Inst. Volcanol. Seismol. Quezon City 413–535. <https://doi.org/10.1159/000153100>
- Pardo, N., Avellaneda, J.D., Rausch, J., Jaramillo-Vogel, D., Gutiérrez, M., Foubert, A., 2020. Decrypting silicic magma/plug fragmentation at Azufral crater lake, Northern Andes: insights from fine to extremely fine ash morpho-chemistry. *Bull. Volcanol.* 82. <https://doi.org/10.1007/s00445-020-01418-z>

Pardo, N., Cronin, S.J., Németh, K., Brenna, M., Schipper, C.I., Breard, E., White, J.D.L., Procter, J., Stewart, B., Agustín-Flores, J., Moebis, A., Zernack, A., Kereszturi, G., Lube, G., Auer, A., Neall, V., Wallace, C., 2014. Perils in distinguishing phreatic from phreatomagmatic ash; insights into the eruption mechanisms of the 6 August 2012 Mt. Tongariro eruption, New Zealand. *J. Volcanol. Geotherm. Res.* 286, 397–414.

<https://doi.org/10.1016/j.jvolgeores.2014.05.001>

Pereira Borges, H., Aguiar, M.S. de, 2019. Mineral classification using machine learning and images of microscopic rock thin section., Mexican international conference on artificial intelligence. Springer, Cham, 2019.

https://doi.org/10.1007/978-3-030-33749-0_6

Polacci, M., Andronico, D., de' Michieli Vitturi, M., Taddeucci, J., Cristaldi, A., 2019. Mechanisms of Ash Generation at Basaltic Volcanoes: The Case of Mount Etna, Italy. *Front. Earth Sci.* 7. <https://doi.org/10.3389/feart.2019.00193>

Primulyana, S., Kern, C., Lerner, A.H., Saing, U.B., Kunrat, S.L., Alfianti, H., Marlia, M., 2018. Gas and ash emissions associated with the 2010-present activity of Sinabung Volcano, Indonesia. *J. Volcanol. Geotherm. Res.*

<https://doi.org/10.1016/j.jvolgeores.2017.11.018>

Qin, X., Zhang, Z., Huang, C., Dehghan, M., Zaiane, O.R., Jagersand, M., 2020. U2-Net: Going deeper with nested U-structure for salient object detection. *Pattern Recognit.* 106. <https://doi.org/10.1016/j.patcog.2020.107404>

- Ross, P.S., Dürig, T., Comida, P.P., Lefebvre, N., White, J.D.L., Andronico, D., Thivet, S., Eychee, J., Gurioli, L., 2022. Standardized analysis of juvenile pyroclasts in comparative studies of primary magma fragmentation; 1. Overview and workflow. *Bull. Volcanol.* 84, 1–29. <https://doi.org/10.1007/s00445-021-01516-6>
- Rowe, M.C., Thornber, C.R., Kent, A.J.R., 2008. Identification and Evolution of the Juvenile Component in. *A Volcano Rekindled Renewed Erupt. Mt. St. Helens, 2004–2006* 2004–2006.
- Scheidegger, K. F., Federman, A. N., and Tallman, A. M., 1982. Compositional heterogeneity of tephra from the 1980 eruptions of Mount St. Helens. *Journal of Geophysical Research: Solid Earth* 87.B13: 10861-10881
- Shoji, D., Noguchi, R., Otsuki, S., Hino, H., 2018. Classification of volcanic ash particles using a convolutional neural network and probability 1–12. <https://doi.org/10.1038/s41598-018-26200-2>
- Singh, S., Srivastava, D., Agarwal, S., 2017. GLCM and its application in pattern recognition. *5th Int. Symp. Comput. Bus. Intell. ISCBI 2017* 20–25. <https://doi.org/10.1109/ISCBI.2017.8053537>
- Smith, L.I., 2002. A tutorial on principal components analysis.
- Spadaro, F.R., Lefèvre, R.A., Ausset, P., 2002. Experimental rapid alteration of basaltic glass: Implications for the origins of atmospheric particulates. *Geology* 30, 671–674. [https://doi.org/10.1130/0091-7613\(2002\)030<0671:ERAOBG>2.0.CO;2](https://doi.org/10.1130/0091-7613(2002)030<0671:ERAOBG>2.0.CO;2)

- Sural, S., Qian, G., Pramanik, S., 2002. Segmentation and histogram generation using the HSV color space for image retrieval. *IEEE Int. Conf. Image Process.* 2, 589–592. <https://doi.org/10.1109/icip.2002.1040019>
- Suzuki, Y., Nagai, M., Maeno, F., Yasuda, A., Hokanishi, N., Shimano, T., Ichihara, M., Kaneko, T., Nakada, S., 2013. Precursory activity and evolution of the 2011 eruption of Shinmoe-dake in Kirishima volcano-insights from ash samples. *Earth, Planets Sp.* 65, 591–607. <https://doi.org/10.5047/eps.2013.02.004>
- Taddeucci, J., Civico, R., Romero, J.E., Burton, M., Francisco, C., Ricci, T., Pankhurst, M.J., Hern, P.A., Llewellyn, E.W., Pistolesi, M., Polacci, M., Solana, C., Auria, L.D., Asensio-ramos, M., 2022. The initial phase of the 2021 Cumbre Vieja ridge eruption (Canary Islands): Products and dynamics controlling edifice growth and collapse 431. <https://doi.org/10.1016/j.jvolgeores.2022.107642>
- Taddeucci, J., Pompilio, M., Scarlato, P., 2004. Conduit processes during the July-August 2001 explosive activity of Mt. Etna (Italy): Inferences from glass chemistry and crystal size distribution of ash particles. *J. Volcanol. Geotherm. Res.* 137, 33–54. <https://doi.org/10.1016/j.jvolgeores.2004.05.011>
- Taddeucci, J., Pompilio, M., Scarlato, P., 2002. Monitoring the explosive activity of the July-August 2001 eruption of Mt. Etna (Italy) by ash characterization. *Geophys. Res. Lett.* 29, 71-1-71–4. <https://doi.org/10.1029/2001GL014372>
- Taddeucci, J., Wohletz, K.H., 2001. Temporal evolution of the Minoan eruption (Santorini, Greece), as recorded by its Plinian fall deposit and interlayered ash

flow beds. *J. Volcanol. Geotherm. Res.* 109, 299–317.

[https://doi.org/10.1016/S0377-0273\(01\)00197-4](https://doi.org/10.1016/S0377-0273(01)00197-4)

Watanabe, Koichiro, Danhara, T., Watanabe, Kazunori, Terai, K., Yamashita, T., 1999.

Juvenile volcanic glass erupted before the appearance of the 1991 lava dome,

Unzen volcano, Kyushu, Japan. *J. Volcanol. Geotherm. Res.* 89, 113–121.

[https://doi.org/10.1016/S0377-0273\(98\)00127-9](https://doi.org/10.1016/S0377-0273(98)00127-9)

Yamanoi, Y., Takeuchi, S., Okumura, S., Nakashima, S., Yokoyama, T., 2008. Color

measurements of volcanic ash deposits from three different styles of summit

activity at Sakurajima volcano, Japan: Conduit processes recorded in color of

volcanic ash. *J. Volcanol. Geotherm. Res.* 178, 81–93.

<https://doi.org/10.1016/j.jvolgeores.2007.11.013>

Summary of supplementary materials

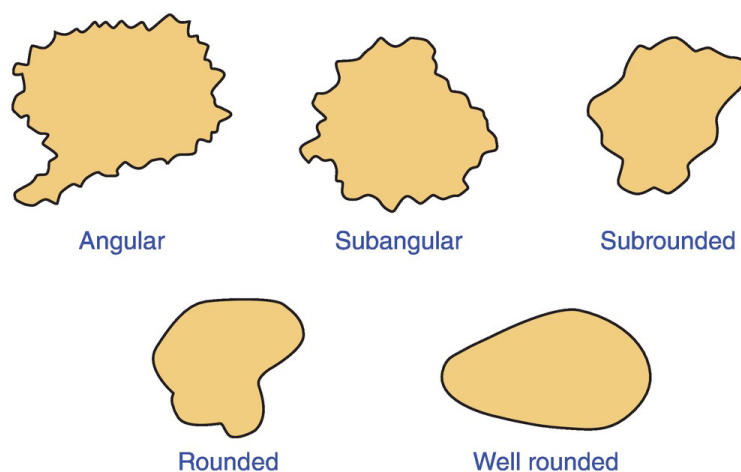


Figure S3.1: Visual comparison chart by Russell, Taylor and Pettijohn (Müller, 1967).

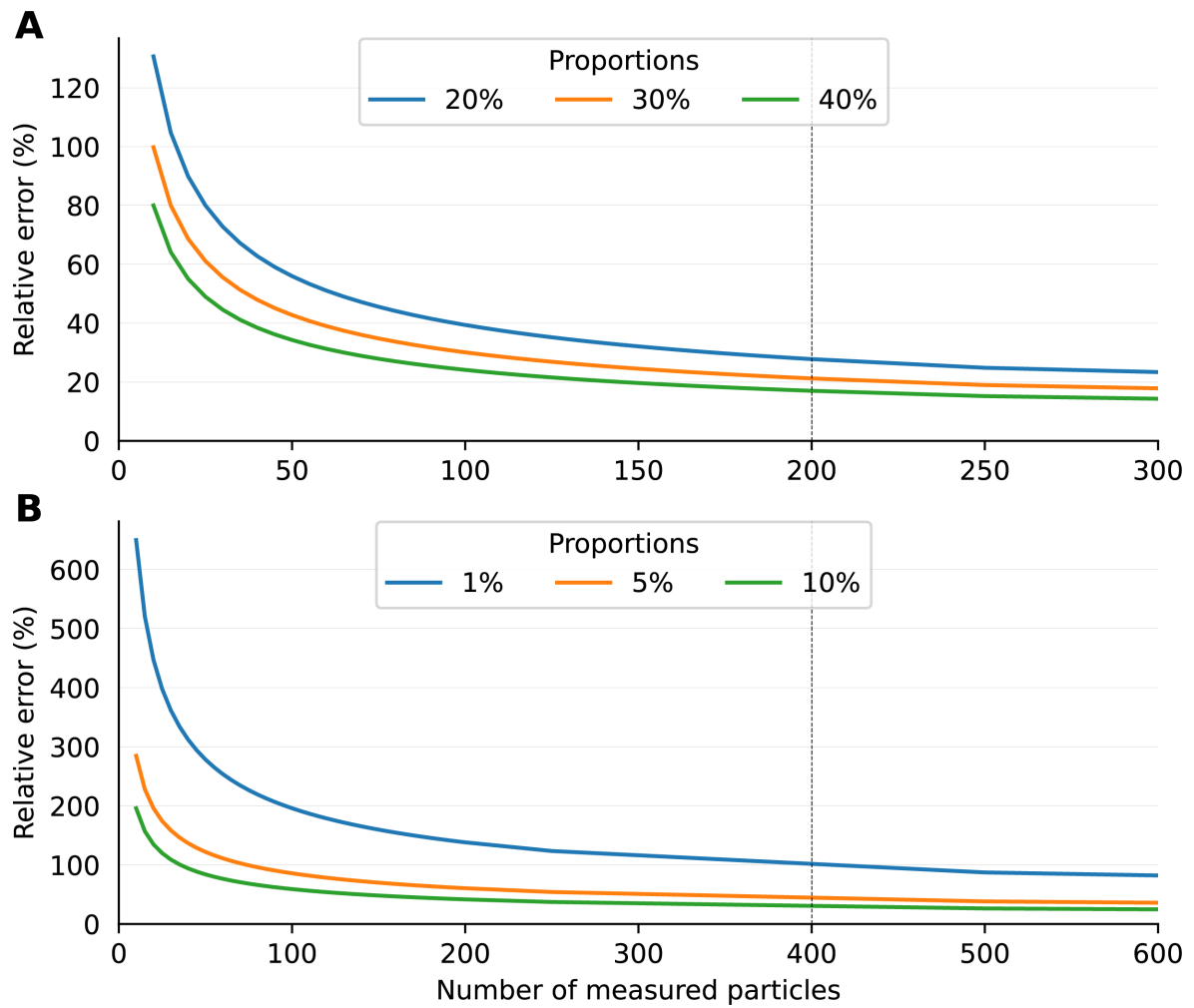


Figure S3.2: Changes of the relative margin of error (ME, Equation 1) at the 95% confidence interval according to the number of measured particles and their different proportions (panel A and B). The dashed vertical lines are for reference, and indicate the number of particles necessary to have a relative error below 30% for proportions > 20% (Panel A), and to have a relative error below 100% for smaller amounts 1–10% (Panel B).

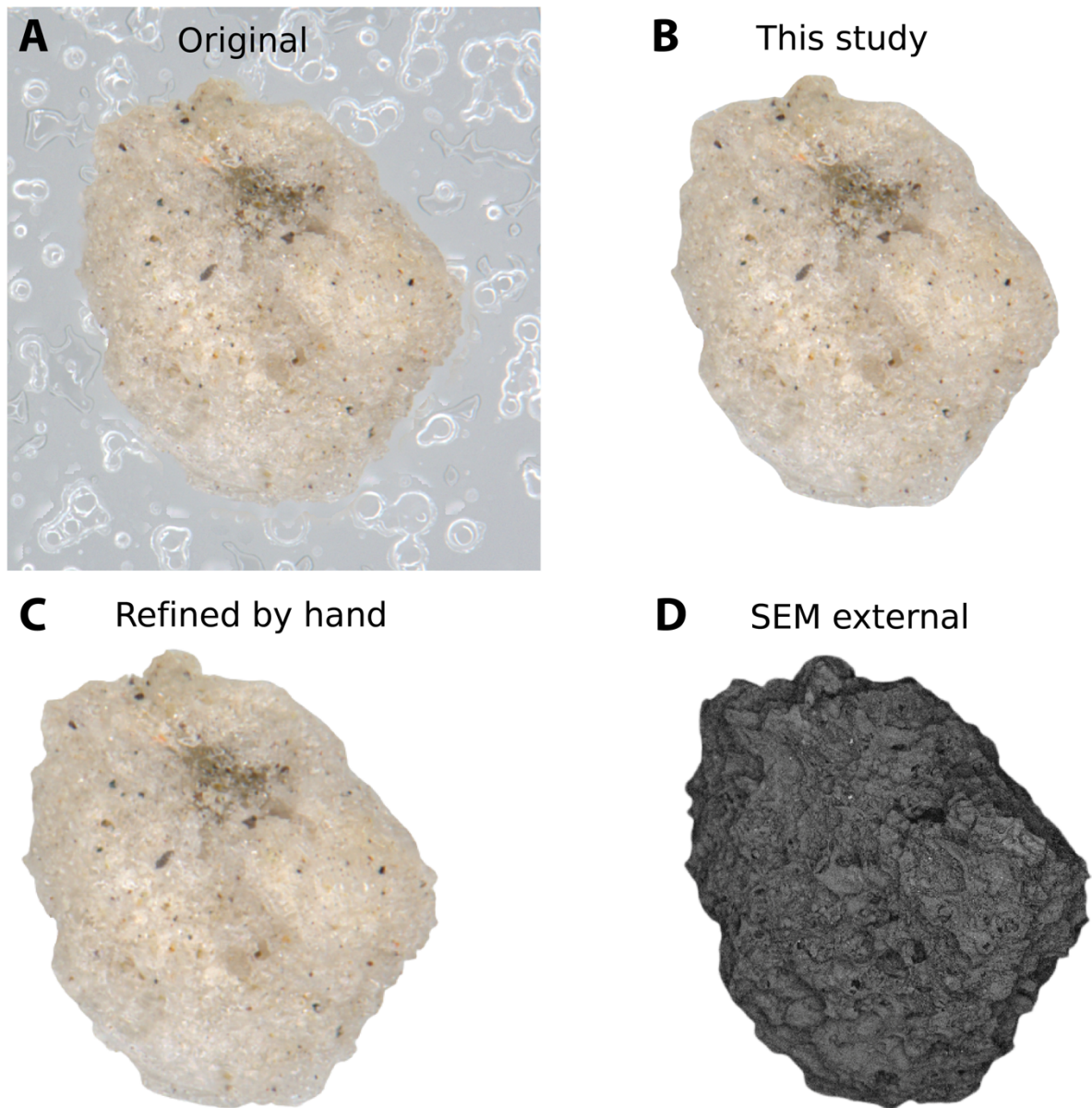


Figure S3.3: Comparison of methodologies for particle segmentation of the same (A) original image. (B) Image used in this study after applying the segmentation algorithm by Qin et al., 2019. Note the smooth outline. Images (C) refined using PhotoShop© and (D) taken of the external shape in the SEM capture more accurately the outline irregularities.

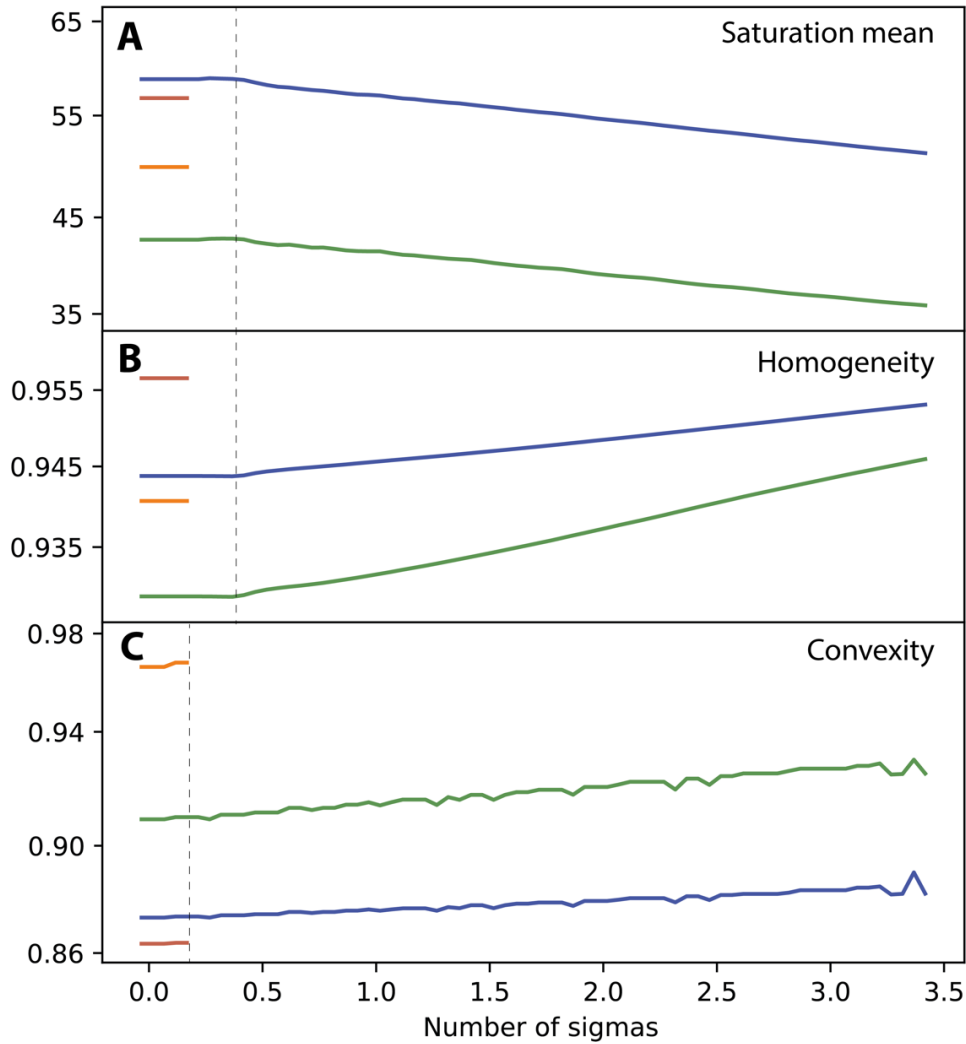


Figure S3.4: Line plots at varying sigmas, which determine the intensity of the blur artificially applied, of (A) the mean of the saturation, which is informative of the overall color purity and intensity, (B) homogeneity, which is sensitive to small pixel values differences, and (C) convexity, which measures the amount that the contour differs from being convex. As the blur increases, the saturation decreases, whereas the homogeneity and convexity increases, the latter with a distinct irregular trend. The

extracted features of the two lighter-colored particles (orange and maroon) are truncated where the algorithm failed to detect the contour, probably resulting from the low contrast.

Table S3.1: Contribution to variance of the extracted features on the 6 principal components extracted for PCA.

	PC1	PC2	PC3	PC4	PC5	PC6
green_mode	-0.200	0.106	-0.006	0.106	-0.023	-0.088
blue_mode	-0.199	0.074	-0.085	0.108	0.062	-0.120
green_mean	-0.199	0.110	-0.017	0.119	-0.022	-0.086
blue_mean	-0.198	0.087	-0.089	0.125	0.048	-0.117
red_mode	-0.197	0.117	0.045	0.108	-0.073	-0.065
red_mean	-0.196	0.124	0.042	0.117	-0.079	-0.056
value_mean	-0.195	0.123	0.039	0.119	-0.076	-0.061
value_mode	-0.194	0.114	0.046	0.116	-0.076	-0.080
homogeneity	-0.187	0.074	0.015	-0.069	0.177	0.136
energy	-0.173	0.059	0.001	0.007	0.211	0.186
circularity_cioni	-0.162	-0.228	-0.130	-0.036	-0.153	0.033
asm	-0.161	0.054	-0.006	0.033	0.232	0.204
solidity	-0.153	-0.199	-0.121	-0.059	-0.228	-0.041
compactness	-0.136	-0.183	0.008	-0.044	-0.177	-0.389
convexity	-0.133	-0.138	-0.310	-0.074	-0.216	0.103
roundness	-0.120	-0.295	0.185	0.065	0.069	-0.004
hue_mean	-0.119	0.127	0.163	0.204	-0.217	0.144
correlation	-0.111	0.006	-0.064	0.265	0.184	0.163
rect_comp	-0.039	-0.080	0.229	0.000	-0.037	-0.633
hue_mode	-0.036	0.066	0.067	0.271	-0.217	0.100
aspect_rat	0.026	0.085	-0.105	-0.046	-0.081	-0.069
saturation_mode	0.050	0.078	0.382	0.006	-0.368	0.195
saturation_mean	0.107	0.043	0.353	-0.010	-0.324	0.187
elongation	0.118	0.297	-0.179	-0.036	-0.057	0.033
rectangularity	0.135	0.153	0.283	0.064	0.214	-0.270
red_std	0.140	-0.083	-0.169	0.398	0.029	-0.028
circ_rect	0.152	0.213	0.189	0.060	0.211	-0.110
green_std	0.157	-0.083	-0.131	0.370	-0.017	-0.021
value_std	0.158	-0.092	-0.149	0.350	0.037	-0.026
circularity_dellino	0.158	0.238	0.123	0.050	0.184	-0.015
blue_std	0.161	-0.068	-0.049	0.343	-0.111	-0.002
hue_std	0.173	-0.154	-0.155	-0.107	0.152	-0.041

contrast	0.180	-0.061	-0.054	0.206	-0.045	-0.020
blue_skew	0.184	-0.086	0.036	-0.127	-0.014	0.018
saturation_std	0.188	-0.058	0.148	0.007	-0.154	0.107
green_skew	0.190	-0.103	0.013	-0.105	-0.020	-0.028
